

Alma Mater Studiorum Università di Bologna  
Archivio istituzionale della ricerca

Genesis of wavy carbonate flowstone deposits in Bossea Cave (North Italy) and their hydroclimatic significance

This is the final peer-reviewed author's accepted manuscript (postprint) of the following publication:

*Published Version:*

Columbu, A., Nannoni, A., Grasso, N., Dabove, P., Fiorucci, A., Vigna, B., et al. (2022). Genesis of wavy carbonate flowstone deposits in Bossea Cave (North Italy) and their hydroclimatic significance. CATENA, 214, 1-15 [10.1016/j.catena.2022.106294].

*Availability:*

This version is available at: <https://hdl.handle.net/11585/883102> since: 2022-04-26

*Published:*

DOI: <http://doi.org/10.1016/j.catena.2022.106294>

*Terms of use:*

Some rights reserved. The terms and conditions for the reuse of this version of the manuscript are specified in the publishing policy. For all terms of use and more information see the publisher's website.

This item was downloaded from IRIS Università di Bologna (<https://cris.unibo.it/>).  
When citing, please refer to the published version.

(Article begins on next page)

This is the final peer-reviewed accepted manuscript of:

Columbu, Andrea; Nannoni, Alessia; Grasso, Nives; Dabove, Paolo; Fiorucci, Adriano; Vigna, Bartolomeo; Bertagni, Matteo B.; Camporeale, Carlo; Forti, Paolo; De Waele, Jo; Spötl, Christoph: *Genesis of wavy carbonate flowstone deposits in Bossea Cave (North Italy) and their hydroclimatic significance*

CATENA VOL. 214 ISSN 0341-8162

DOI: 10.1016/j.catena.2022.106294

The final published version is available online at:

<https://dx.doi.org/10.1016/j.catena.2022.106294>

Terms of use:

Some rights reserved. The terms and conditions for the reuse of this version of the manuscript are specified in the publishing policy. For all terms of use and more information see the publisher's website.

This item was downloaded from IRIS Università di Bologna (<https://cris.unibo.it/>)

**When citing, please refer to the published version.**



## Genesis of wavy carbonate flowstone deposits in Bossea cave (North Italy) and their hydroclimatic significance

Andrea Columbu<sup>a,\*</sup>, Alessia Nannoni<sup>b,c</sup>, Nives Grasso<sup>d</sup>, Paolo Dabove<sup>d</sup>, Adriano Fiorucci<sup>d</sup>, Bartolomeo Vigna<sup>d</sup>, Matteo B. Bertagni<sup>e</sup>, Carlo Camporeale<sup>d</sup>, Paolo Forti<sup>b</sup>, Jo De Waele<sup>b</sup>, Christoph Spötl<sup>f</sup>

<sup>a</sup> Department of Chemistry, Life Sciences and Environmental Sustainability. University of Parma, Parco Area delle Scienze 157A, 43124 Parma, Italy

<sup>b</sup> Department of Biological, Geological and Environmental Sciences, University of Bologna, Via Zamboni 67, 40126 Bologna, Italy

<sup>c</sup> Department of Earth Sciences, University of Florence, Via La Pira 4, 50121, Florence, Italy

<sup>d</sup> Department of Environment, Land and Infrastructure Engineering (DIAI), Polytechnic of Turin, Corso Duca degli Abruzzi 24, 10129 Torino, Italy

<sup>e</sup> High Meadow Environmental Institute, Princeton University, Princeton University, Princeton, NJ 08544, USA

<sup>f</sup> Institute of Geology, University of Innsbruck, Innrain 52, 6020 Innsbruck, Austria

### ARTICLE INFO

#### Keywords:

Calcite speleothems  
Palaeoclimate  
Hydrogeology  
Terrestrial laser scanning  
Stable isotopes  
Fluid flow modelling

### ABSTRACT

Speleothems show an array of shapes. Flowstones are commonly tabular sheet-like deposits, which cover cave floors and walls. They can procure detailed information about past hydrogeological conditions through their morphology, geochemical composition and stratigraphic properties, which in turn are related to the climate conditions at the surface. This is possible if the climate and environmental factors controlling the formation of these deposits are well understood. In Bossea Cave (north-east Italy), we have investigated highly symmetrical wavy flowstones that have never been described in detail before. These deposits show a cyclical repetition of sloped and sub-vertical layers, with knickpoints migrating downslope. This paper investigates the origin of these peculiar carbonate deposits, using: i) terrestrial laser scanning surveys; ii) petrographic observations; iii) oxygen and carbon stable isotope analyses; iv) hydrochemical monitoring data of feeding waters. According to these analyses, we have generated a genetic model that demonstrates: 1) laminar flow of  $\text{CaCO}_3$ -rich water prevails during the deposition of the flowstone; in accordance, the final flowstone architecture does not appear to be influenced by random irregularities of the underlying bedrock substrate. 2) The peculiar morphology is inherited by ripples occurring in the flowing water films during carbonate deposition, which trigger the precipitation of regularly spaced  $\text{CaCO}_3$  deposits along the bedrock slopes. Because of these ripple-induced initial deposits, calcite then deposits as sloped and sub-vertical layers, giving rise to a wavy-like morphology. 3) Wavy calcite layers are only deposited after heavy rainfall events occurred within two to four consecutive rainy days (10 to 20 mm/hour during rainfall peaks; average rates between 3.5 and 7.0 mm/hour); in contrast, calcite deposition cannot occur during low rainfall events (less than 5 mm/hour during rainfall peaks, average rates around 0.8 mm/hour). We therefore propose that the studied wavy flowstones are hydroclimatic indicators, testifying the occurrence of flashy type recharge related to heavy rainfall events. Similar deposits could record these same hydro-climatic conditions in other karst areas.

In recent decades, storms have caused more frequent flooding in highly populated Mediterranean areas, especially in Italy. Wavy flowstones may offer a new archive to gain a better understanding of the long-term dynamics of intense precipitation events and, thus, help to improve future climate scenarios.

\* Corresponding author.

E-mail addresses: [andrea.columbu@unipr.it](mailto:andrea.columbu@unipr.it) (A. Columbu), [alessianannoni@gmail.com](mailto:alessianannoni@gmail.com) (A. Nannoni), [nives.grasso@polito.it](mailto:nives.grasso@polito.it) (N. Grasso), [paolo.dabove@polito.it](mailto:paolo.dabove@polito.it) (P. Dabove), [adriano.fiorucci@polito.it](mailto:adriano.fiorucci@polito.it) (A. Fiorucci), [bartolomeo.vigna@polito.it](mailto:bartolomeo.vigna@polito.it) (B. Vigna), [matteobb@princeton.edu](mailto:matteobb@princeton.edu) (M.B. Bertagni), [carlo.camporeale@polito.it](mailto:carlo.camporeale@polito.it) (C. Camporeale), [paolo.forti@unibo.it](mailto:paolo.forti@unibo.it) (P. Forti), [jo.dewaele@unibo.it](mailto:jo.dewaele@unibo.it) (J. De Waele), [christoph.spoetl@uibk.ac.at](mailto:christoph.spoetl@uibk.ac.at) (C. Spötl).

<https://doi.org/10.1016/j.catena.2022.106294>

Received 4 August 2021; Received in revised form 15 February 2022; Accepted 6 April 2022  
0341-8162/© 20XX

## 1. Introduction

Speleothems are chemically precipitated cave deposits (Moore, 1952), mostly composed of calcite (White, 1976). They form when carbonate-rich seepage waters in karst systems become supersaturated with respect to  $\text{CaCO}_3$  because of the loss of  $\text{CO}_2$  and/or evaporation (Forti and Hill, 2004). The size, morphology, and fabric of speleothems depend on various factors, such as flow characteristics, degree of supersaturation and physicochemical properties of the feeding water (Fairchild and Baker, 2012). Field and laboratory experiments have allowed to model the evolution of these deposits through time, according to changes in the hydrodynamic and geochemical conditions of the feeding water (Curl, 1973; Dreybrodt and Romanov, 2008). Speleothems are highly sought palaeoenvironmental and palaeoclimate archives (Henderson, 2006), because 1) they can be radiometrically dated with high accuracy and precision (Richards and Dorale, 2003; Hellstrom, 2006), 2) their geochemical and physical properties often respond to climate variations above the cave (Fairchild et al., 2006; Lachniet, 2009), and 3) caves are present at almost all latitudes, longitudes and altitudes (Lechleitner et al., 2018; Atsawawaranunt et al., 2018). Understanding the processes of speleothem formation is thus fundamental to sustain, integrate and reinforce the interpretation of palaeoenvironmental/climate proxy time series (Muñoz-García et al., 2016; Martín-Chivelet et al., 2017).

Speleothem-based palaeoenvironmental and palaeoclimate reconstructions have mostly been based on stalagmites (Cheng et al., 2016). Less commonly flowstones, i.e. sheet-like deposits formed from diffuse water flow on cave walls and floors, have been used (Columbu et al., 2019; Drysdale et al., 2020; Gázquez et al., 2018; Hellstrom and McCulloch, 2000). With respect to palaeoclimate research, stalagmites and flowstones have both pros and cons (Fairchild and Baker, 2012). A distinct advantage of flowstones is their commonly much larger volume and size, allowing for sampling (by coring) without significantly affecting the integrity of the cave (Columbu et al., 2021). In contrast, sampling stalagmites usually requires their complete removal from the

cave. Flowstones locally also occur in non-karstic (carbonate-poor) rocks, enlarging their potential as palaeoenvironmental and palaeoclimatic archives (Koltai et al., 2018; Sanjurjo-Sanchez et al., 2021).

Little attention has been paid to the processes leading to flowstone formation, although studies have shown that their bedding geometry, fabrics as well as their geochemical properties can be rather complex (Hellstrom and McCulloch, 2000; Frisia, 2015). This also applies to their morphology, which can vary on a range of scales. Here, we document flowstones from Bossea Cave (northwest Italy), characterised by an extremely symmetrical and regular wavy growth pattern. We performed 3D surveys using laser scanning techniques, as well as petrographic and oxygen and carbon stable isotope analyses to elucidate their origin. The results were compared to hydrological monitoring data thanks to the existence of a unique hydrogeological cave laboratory, which has been in operation since more than 30 years (Vigna et al., 2017). This study thus presents a comprehensive evolutionary model for wavy flowstones, aiming to unravel the hydroclimate conditions leading to their deposition. This type of speleothem may be more widespread than previously thought (e.g., Forti et al., 2017), hence procuring a novel tool for the study of climate-driven hydrological variations in karst areas.

## 2. Study area

### 2.1. Geological setting

Bossea cave is located in the Ligurian Alps at an altitude of 828 m a.s.l. in southern Piedmont, NW Italy (Fig. 1a). It represents the terminal part of a karst catchment that drains water from the Corsaglia and Maudagna valleys (Nannoni et al., 2020; Fig. 1b). Its downstream part is a show cave visited by ~ 30,000 tourists each year. Ongoing research on karst hydrology and cave climatology is carried out by means of two underground laboratories that are managed by the local section of the Italian Alpine Club (CAI) and the Polytechnic University of Turin (Vigna et al., 2017; Fig. 2).

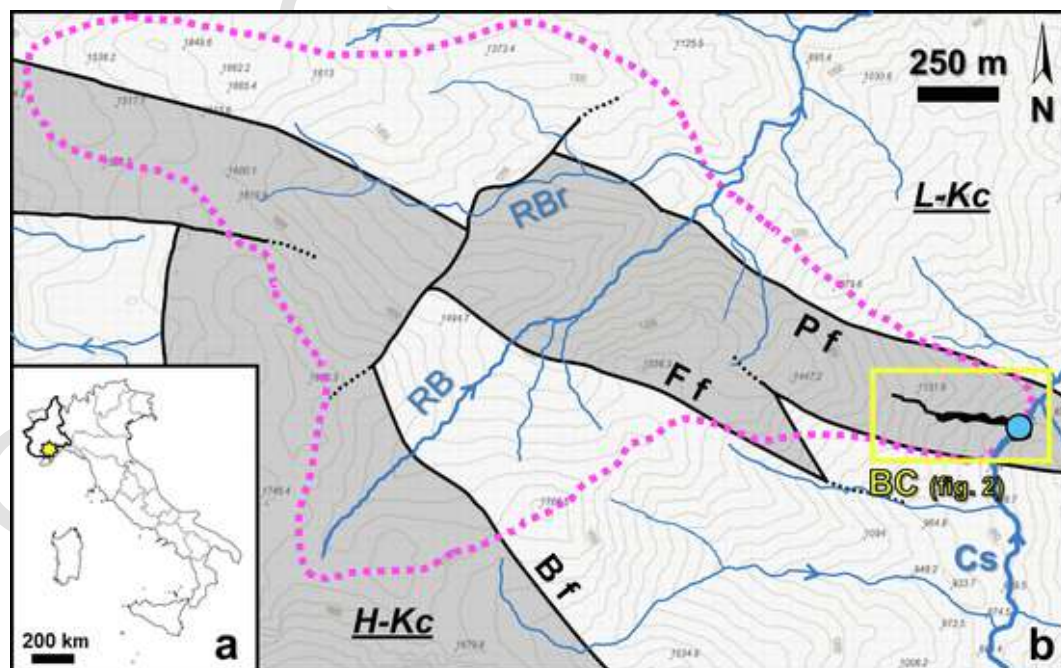


**Fig. 1.** Study area. (a) Location of the Bossea cave marked by a yellow star within the Piedmont region of NW Italy (bold black outline). (b) Simplified hydrogeological map of the study area showing the location of the Bossea cave (BC, yellow rectangle), the Bossea catchment (pink dotted line), the Bossea spring (blue circle), and the location of faults (black lines). Labels: B/F/P f = Borello, Fontane and Prel faults, Cs = Corsaglia stream, RB = Roccia Bianca brook, RBr = Bertino brook, L/H-Kc = low/high-hydraulic conductivity complex. Modified after Nannoni et al. (2020). (For interpretation of the references to colour in this figure legend, the reader is referred to the web version of this article.)

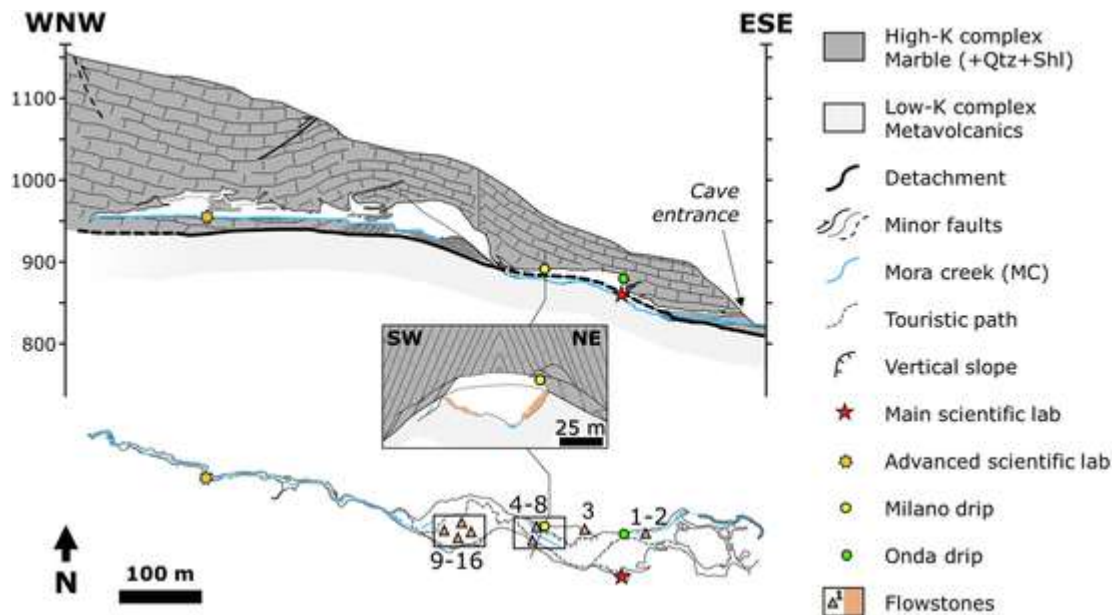


**Fig. 2.** WNW-ESE cross-section (top) and plan view of the Bossea cave (bottom). The inset shows a NE-SW geological cross-section along the area where the Milano drip and several massive and wavy flowstones are located. The numbers close to the orange triangles refer to the studied flowstones (modified after Antonellini et al., 2019). (For interpretation of the references to colour in this figure legend, the reader is referred to the web version of this article.)

The main underground stream, the Mora creek (MC, Fig. 2), has a discharge varying between 60 and 1960 l/s and is fed by several secondary tributaries (discharge less than 1 l/s) that drain water from a 60 to 100 m-thick vadose zone (Nannoni et al., 2020).

The structural setting of Bossea cave is controlled by sub-vertical faults related to the Alpine orogenesis (Borello, Fontane, and Prel faults) that resulted in metamorphic Mesozoic carbonate rocks (calcite and dolomite marble) standing in lateral and vertical contact with metamorphic Permian clastic and volcanoclastic rocks (Antonellini et al., 2019). A hydrogeological model was established, consisting of fault-controlled blocks made up mostly of marble (termed “high-hydraulic conductivity complex” (H-Kc)), and units composed predominantly by shales, metavolcanics, and quartzite (called “low-hydraulic conductivity complex” (L-Kc), Fig. 1). The show cave part develops along a detachment between an isoclinally folded sequence of marble, quartzite and shale, and the underlying metavolcanics. The Mora creek flows along this detachment in the downstream sector of the cave, eroding the heavily deformed metavolcanics and leading to the development of large rooms (Antonellini et al., 2019). Metavolcanics outcrop in the cave where they are not covered by speleothems, showing rather smooth, slightly irregular and steep slopes.

The presence of the underground river and the limited connection to the outside atmosphere (Bossea cave has only one rather small entrance) causes the cave atmosphere to be constantly saturated with respect to water vapour (100% relative humidity) and in many places condensation occurs.

Massive flowstone deposits cover the sides of the large rooms (Figs. 2 and 3), organised in multiple steps. These flowstones are fed by secondary tributaries that discharge water either along the detachment zone or via drip sites located on the carbonate ceiling. Some of these tributaries have been monitored (sections 2.2 and 4).

The landscape above the cave is characterised by steep SE-facing slopes with bare rock outcrops and a thin soil cover. The steep morphology at the surface limits infiltration, especially during heavy storms (Nannoni et al., 2020).

## 2.2. Hydrology and hydrochemistry of the unsaturated (vadose) inflows

The hydrological behaviour of the secondary tributaries is controlled by the architecture of the unsaturated zone and by the local climate (Nannoni et al., 2020). The latter is characterised by heavy snowfall during winter followed by heavy rainfall in spring/autumn and snow melting in spring. Infiltration is low during occasional summer storms due to high evapotranspiration, whereas it is high during autumn (which is the rainiest season) and spring (because of snow melt). Mean annual precipitation ranges between 1100 and 1200 mm. The secondary tributaries show a piston-flow behaviour during infiltration events so that hydraulic pressure is quickly transmitted through the water-conductive fracture network (Nannoni et al., 2020). Therefore, water is stored during intervals of no precipitation and reaches thermal and chemical equilibrium with the carbonate host rock. Tracer tests showed that the unsaturated zone feeding the secondary tributaries is characterised by a dispersed circulation system (see below), in which water is stored in the most fractured portions of the carbonate rocks. The unsaturated fracture flow is characterised by a maximum flow velocity of 30–60 m/day and long recovery times (more than a month) (Banzato et al., 2013). The tributaries classify as Ca-HCO<sub>3</sub> or Ca-Mg-HCO<sub>3</sub> water types (Nannoni et al., 2020).

## 3. Material

Flowstones showing a wavy morphology are present throughout the cave, especially in the large central chamber (Figs. 2, 3 and 4). In total, 16 deposits were mapped (Figs. 2 and 4) and surveyed by 3D technology (see below). Although dry during surveys, the flowstones were actively growing during wet periods in past years. According to field observations, the flowstones are covered by a continuous water film after heavy storms, whereas common seepage only causes rivulet-like water on the flowstone surface (Fig. 3).

A 4 cm-thick and ~ 55 cm-long slice of a flowstone from a scarcely visible part of the central room was cut using an electric handheld diamond circular saw. The slice runs perpendicularly to the speleothem growth direction. During slicing we encountered the presence of powdery moonmilk at its base (where the slice broke during cutting), which, however, could not be sampled for further analyses. The flow-



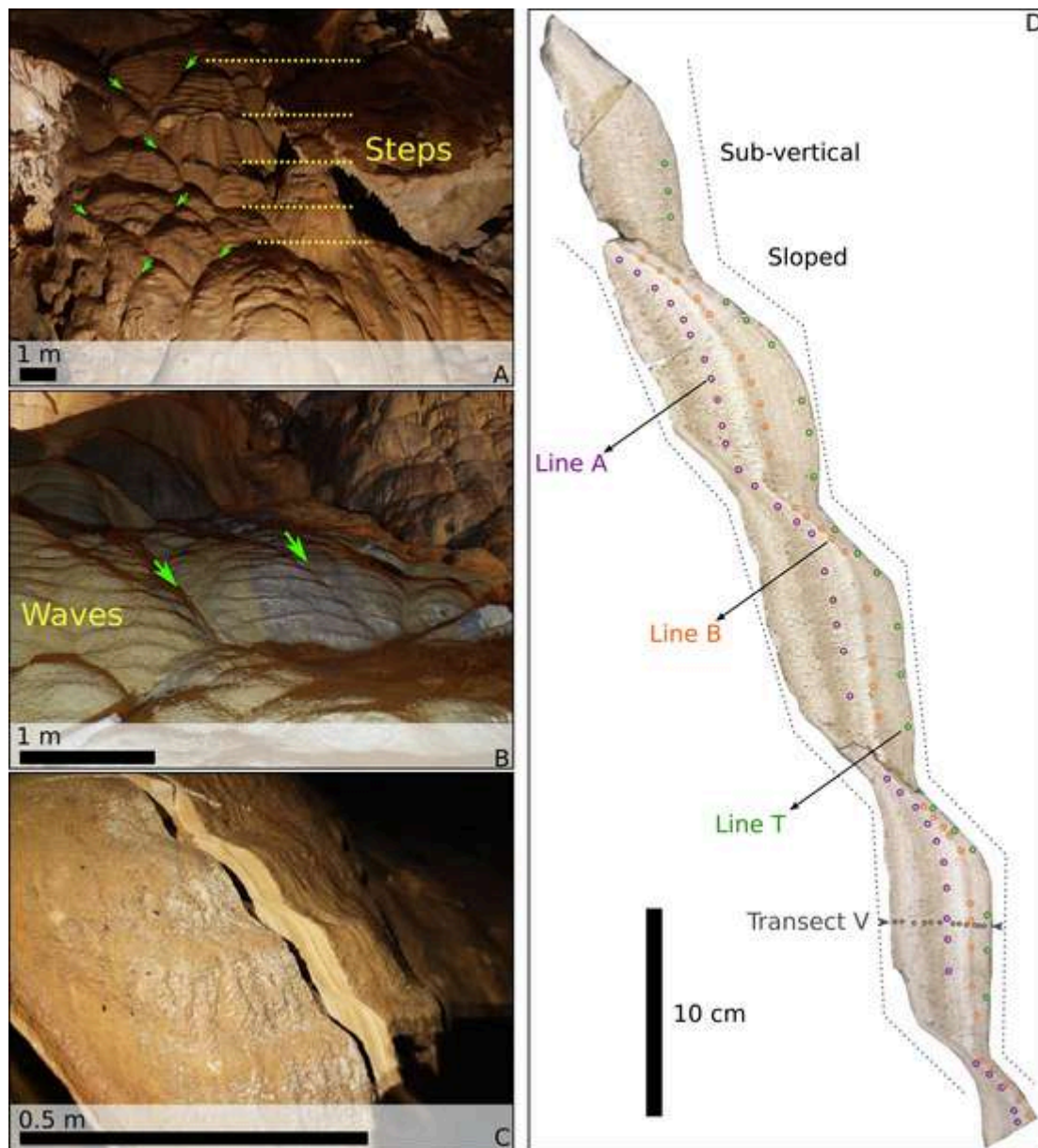


**Fig. 3.** The studied flowstone showing steps (A) and a regular wavy morphology (B, C). (C) Sampling location (in the cluster 9–16 in Fig. 4). (D) Longitudinal cross-section of the flowstone showing locations of stable isotope analyses (line A, B and T) along growth layers as well as along a profile (line V). Water covers the entire speleothem surface during episodes of heavy rainfall, while average precipitation only causes rivulet-like water on the speleothem surface (green arrows in A and B point to drainage paths). (For interpretation of the references to colour in this figure legend, the reader is referred to the web version of this article.)

stone hand specimen appears brownish and whitish. The wavy nature of the deposit is clearly visible revealing an alternation of sub-vertical and sloped segments (Fig. 3). The sub-vertical segments are layered and mostly composed of soft porous calcite. More compact and hard layers are intercalated. The more compact layers can be traced to the sloped segments. The latter are composed of hard calcite showing lamination.

## 4. Methods

### 4.1. 3D survey

A laser scanning survey of the entire cave was accomplished in order to precisely map the 16 wavy flowstone deposits. 87 scans were acquired using a Faro Focus Cam2 3D instrument. Each scan was acquired with 1 point every 7 mm at 5 m distance, requiring about 7 minutes for cloud acquisition and 1 minutes for image collection.

For the registration of the point clouds, some markers, spread over the acquisition areas, were surveyed using topographic instruments. Firstly, a reference network outside Bossea cave was established using Global Navigation Satellite System (GNSS) techniques to define high-precision coordinates of the measured points. A GNSS double frequency and multi-constellation receiver was used in static mode collecting data at each point for about 60 min. The total station was then employed to realise a network of points and to measure the position of the markers inside the cave. These measurements were subsequently adjusted using the MicroSurveyStarNet v.7.0 software, which allowed to determine the coordinates of the markers with an accuracy of 1 mm. The laser data were registered using Scene, an in-house software developed by FARO, with a registration error of about 10 mm, compatible with the accuracy of the topographic network and the instrument itself.

The point cloud of the cave was used to analyse the characteristic wavy morphology of the 16 flowstones (Fig. 4). Topographic profiles of each of these deposits were obtained by sectioning the 3D geo-

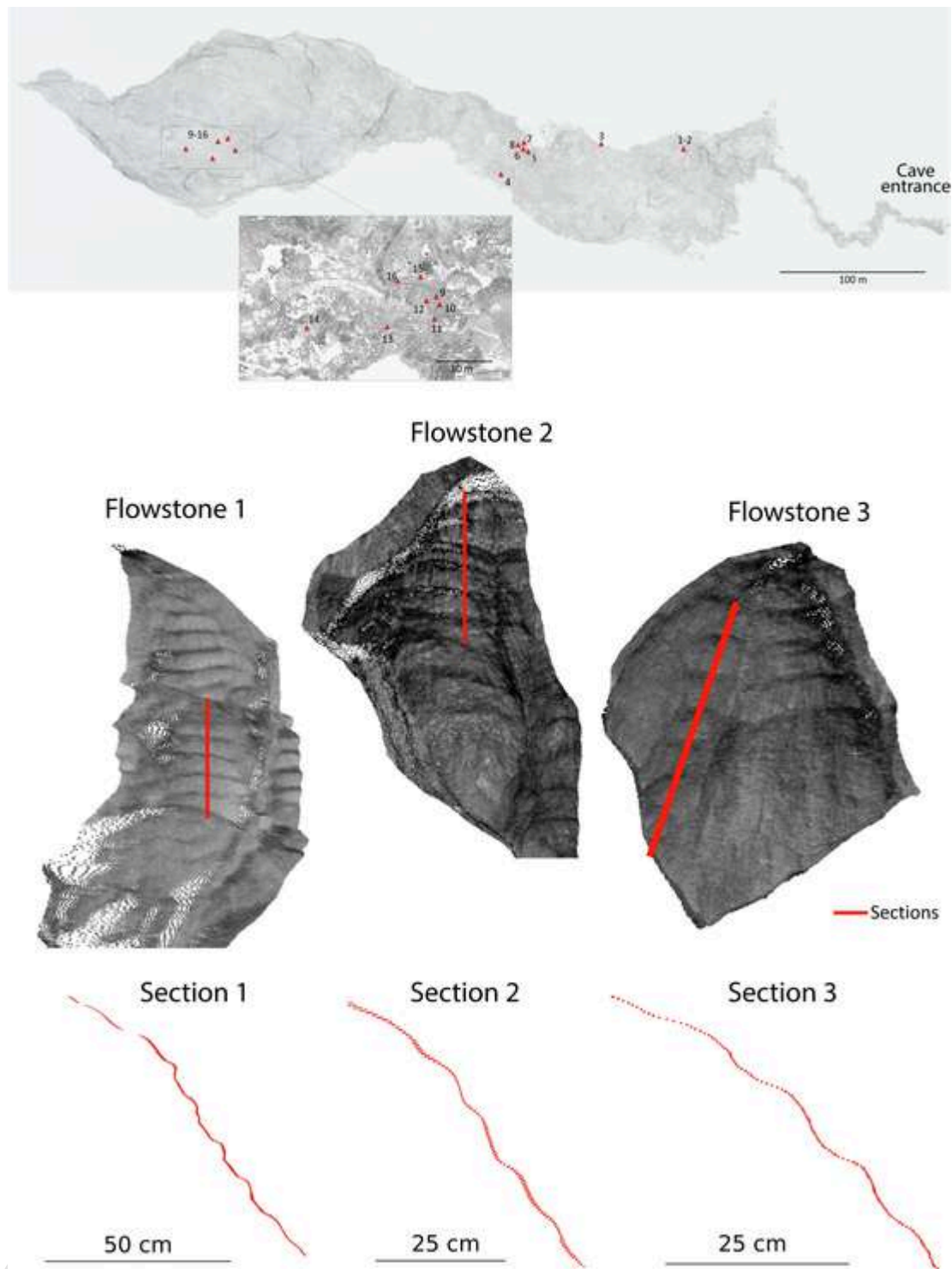


**Fig. 4.** Location of the 16 wavy flowstones (upper panel) extracted from the laser scan survey. The middle panel shows an example of the extraction of point cloud data for individual flowstones, in this case flowstones 1 to 3. Parameters such as wavelength, wave amplitude and slope were obtained along a defined section (red line). An example of the obtained sections is provided in the lower panel. All sections are given in Sup. Fig. 1. (For interpretation of the references to colour in this figure legend, the reader is referred to the web version of this article.)

referenced point cloud with a plane perpendicular to the X-Y plane with the surface of the structure in the centre line and parallel to the Z axis (the red line in Fig. 4). For this purpose, the open source software Cloudcompare was used. For each of these lines a profile of 1–2 cm was extracted, depending on the density of the point cloud in order to obtain sufficient information to characterise the external morphology of these deposits. The 2D contour was computed by projecting each profile

onto its best fit plane, calculated by the software. The contours were then analysed in order to measure some properties of the wavy flowstone surfaces, such as the overall length of the flowstone and, for each wave, its length, amplitude and inclination with respect to the X-Y plane.

## 4.2. Thin section petrography and stable isotope analysis

Thin sections were prepared at Bologna University, BiGeA department, and examined using a Nikon Eclipse Ci-Pol binocular microscope equipped with a digital DS-Fi2-L3 camera.

Subsamples for oxygen and carbon stable isotopes analyses were drilled along three prominent horizontal layers (lines A, B and T) (Fig. 3). The spacing between subsamples was  $\sim 1.5$ – $2.0$  cm along the sub-vertical portions of the speleothem and  $\sim 1$  cm along the sloped ones. Five subsamples were drilled for each sub-vertical/sloped segment for lines A and B, and three subsamples for line T. Additional subsamples were drilled along a transect perpendicular to the growth layers (e.g. line V) (Fig. 3), with a variable spacing of  $0.3$ – $0.5$  cm. This transect represents the stable isotopic variation from the stratigraphic bottom to top, hence through time. For the interpretation of isotopic variation along this transect we also refer to those subsamples drilled along lines A, B and C that are intercepted by line V.

A total of 103 subsamples were drilled and the powders were dissolved in 99% orthophosphoric acid at  $72^\circ\text{C}$  and the resulting  $\text{CO}_2$  was prepared in a Gasbench II and subsequently analysed using a ThermoFisher DELTAplusXL isotope ratio mass spectrometer at the Institute of Geology, University of Innsbruck. Calibration was accomplished using international calcite standards (NBS18, NBS19, CO1, CO8) and the results are reported in permil ( $\text{‰}$ ) notation on the Vienna Pee Dee Belemnite (VPDB) scale. Further analytical details can be found in Koltai et al. (2018).

## 4.3. Hydrology and hydrochemistry

Rainfall data were obtained from the Borello meteorological station of the Piedmont Regional ARPA agency, located  $1.5$  km south with respect to Bossea Cave (Nannoni et al., 2019). The hydrological and hydrochemical behaviour of the Milano drip site (Fig. 2) during consecutive storm events between 7th October and 4th November 2018 is used as an example of the flow dynamics that feeds the flowstones of Bossea cave. The drip site was equipped with a concrete weir and an OTT multiparametric sensor for water discharge, electrical conductivity and temperature. An automated water sampler (ISCO 2900 sampler) was used during the autumn 2018 storm events. The device sampled every 6 h during the first and the second surveys (2018/10/08 22:00 to 2018/10/14 16:00 and 2018/10/15 11:00 to 2018/10/21 11:00) and every 8 h during the third survey (2018/10/25 16:30 to 2018/11/02 16:30; Nannoni et al., 2019).

Water samples were also collected upstream and downstream with respect to an active wavy carbonate flowstone fed by a drip (Onda drip site, Fig. 2) to get insights into the dynamics of calcite precipitation. This drip has a hydrochemical and hydrological behaviour similar to the Milano drip site. pH and temperature were determined on site. Samples collected by the automatic sampler were analysed for major cations and anions at the Laboratory of Hydrogeology of the Polytechnic University of Turin. Determination of  $\text{Ca}^{2+}$  and  $\text{Mg}^{2+}$  was carried out by means of ion-selective electrodes,  $\text{HCO}_3^-$  was determined by acid-base titration and instrumentally controlled pH. Anion concentrations were determined by ion chromatography (Metrohm 881bIC Pro).  $\text{Na}^+$  and  $\text{K}^+$  were determined by atomic absorption spectroscopy, and  $\text{NH}_4^+$  was analysed by UV–VIS spectrophotometry. More information on the analytical procedures can be found in Nannoni et al. (2020). The calcite saturation index (SI) was calculated using WEB-PHREEQ (<https://www.ndsu.edu/webphreeq>), a web implementation of the aqueous geochemical modelling program PHREEQC (Parkhurst & Appelo, 2013).

## 5. Results

### 5.1. Morphology

The wavy flowstone covers cave walls up to  $10$  m high (Fig. 3). The 16 surveyed flowstone sites are characterised by single or multiple steps, forming a more or less convex flowstone segment with the typical wavy appearance (Fig. 3); at least one step of each flowstone was fully covered by the 3D survey. Results are reported in supplementary table 1, comprehensively shown in supplementary Fig. 1 and summarised in Fig. 5. The steps show an average length of  $1.05$  m (min:  $0.48$  m; max:  $1.86$  m). Shorter steps are composed of a smaller number of waves, and vice versa (suppl. table 1). For example, flowstone 3 (length of the surveyed step  $0.48$  m) comprises 4 waves, whereas the surveyed step in flowstone 4, which is three times higher ( $1.28$  m), is composed of 12 waves. Average wavelength, amplitude and slope of the waves are  $0.13$  m (min:  $0.04$  m; max:  $0.24$  m),  $0.02$  m (min:  $0.00$  m; max:  $0.07$  m) and  $45^\circ$  (min:  $5^\circ$ ; max:  $70^\circ$ ), respectively. The wave slope generally increases downstream of each wavy step (Fig. 5b). While the slope of the most upstream waves is always less than  $35^\circ$ , it can reach  $\sim 70^\circ$  in the most downstream portion (Fig. 5b). Slope and wavelength are weakly negatively correlated ( $r = -0.33$ ) (Fig. 5c), and the wavelength decreases accordingly in the downstream direction (suppl. table 1). The wave amplitude is independent of the slope ( $r = -0.23$ ) (Fig. 5d), but is weakly correlated with the wavelength ( $r = 0.34$ ) (suppl. Table 1).

### 5.2. Petrography

The flowstone is composed of dendritic and compact columnar calcite (Frisia, 2015) (Fig. 6). The former fabric only appears in the sub-vertical portions (Fig. 6a–h) characterised by elevated porosity and the presence of detrital particles. The growth of branching polycrystals favours the formation of intercrystalline pores, which result in a porous macroscopic appearance (Frisia and Borsato, 2010). Fine detritus and micrite can be found at the base of the dendrites (Fig. 6g–h). Dendritic fabric alternates with compact calcite fabric (Fig. 6a–d). The latter is the only calcite fabric in the more gently sloping sectors (Fig. 6i–l).

### 5.3. Stable isotopes and water chemistry

With the intent of characterising the stable isotopic composition during single (i.e. synchronous) depositional events, Fig. 7 shows the results of  $\delta^{13}\text{C}$  and  $\delta^{18}\text{O}$  along lines A ( $n = 35$ ), B ( $n = 35$ ) and T ( $n = 20$ ), i.e. within individual growth layers.  $\delta^{13}\text{C}$  and  $\delta^{18}\text{O}$  variations are small along the three lines, i.e. equal or less than  $0.6 \text{ ‰}$  and  $0.4 \text{ ‰}$  for  $\delta^{13}\text{C}$  and  $\delta^{18}\text{O}$ , respectively.  $\delta^{13}\text{C}$  and  $\delta^{18}\text{O}$  are not statistically correlated in these lines. The transect of line V (which cuts perpendicularly along the calcite layers) yielded  $\delta^{13}\text{C}$  (min:  $-10.4 \text{ ‰}$ , max  $-8.7 \text{ ‰}$ ) and  $\delta^{18}\text{O}$  values (min:  $-9.4 \text{ ‰}$ , max:  $-8.9 \text{ ‰}$ ) characterised by a higher variability with respect to lines A, B and T; additionally,  $\delta^{13}\text{C}$  and  $\delta^{18}\text{O}$  values of line V are positively correlated ( $r = 0.64$ ,  $n = 11$ ) (Fig. 8). All isotopic data are available in supplementary table 2.

The Borello meteorological station recorded a total of  $91.8$  mm of rain during the first storm event (10th–11th of October), with average rates of  $7.06$  mm/hour and rainfall well above  $10$  mm/hour during the storm peaks. The second monitored rainfall event (16th–18th of October) was characterised by lower amounts ( $37$  mm) and average rates ( $0.77$  mm/hour); peaks never reached  $5$  mm/hour. Storms occurred again during the third event (27th October–4th November), with a total amount of rainfall around  $159$  mm and average rates at  $3.57$  mm/hour; this storm produced  $\sim 10$  mm/hour of rainfall during peaks.

During the monitored events the water at the Milano drip site classifies as  $\text{Ca-Mg-HCO}_3$  type ( $\text{Ca}^{2+} \approx \text{Mg}^{2+} \gg \text{Na}^+ + \text{K}^+$  to  $\text{Ca}^{2+} > \text{Mg}^{2+} \gg \text{Na}^+ + \text{K}^+$ ). Electrical conductivity ranges between  $400$  and  $520 \mu\text{S/cm}$  and hence represents mineralised water (Nannoni et al.,



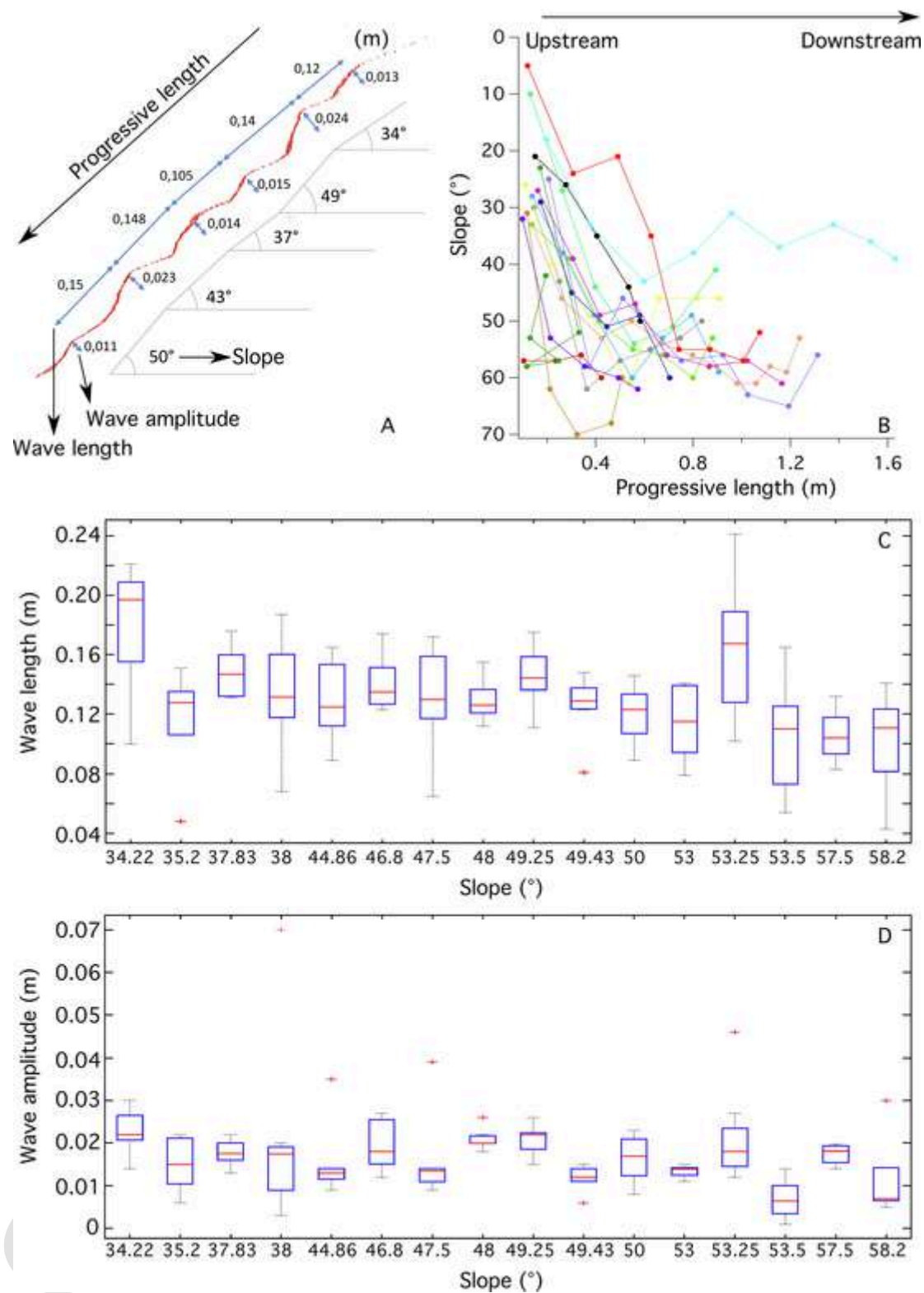


**Fig. 5.** Summary of the main geometrical parameters of the 16 flowstone deposits studied by laser scanning. Values of wave slope, length and amplitude (A) were extracted along discrete sections. The slope is compared to the length of the flowstone (B), wavelength (C) and wave amplitude (D). In A, different colours refer to the 16 flowstones analysed, while dots refer to individual waves.

2020). The first storm event (10th–11th of October) and the subsequent discharge peak marked the onset of autumnal recharge, characterised by a sharp, short-lived response to precipitation (Fig. 9). The second discharge peak followed a weak rainfall event (16th–18th of October), whereas the discharge peaks at the end of October followed multiple

storm events that led to a strong increase in discharge (up to 0.43 l/s). (Fig. 9). Temperature and electrical conductivity data suggest a piston flow-behaviour during all monitored infiltration events (Nannoni et al., 2019). The Mg/Ca ratio and the calcite saturation index document that the water discharged during the second event had a higher Mg/Ca ratio

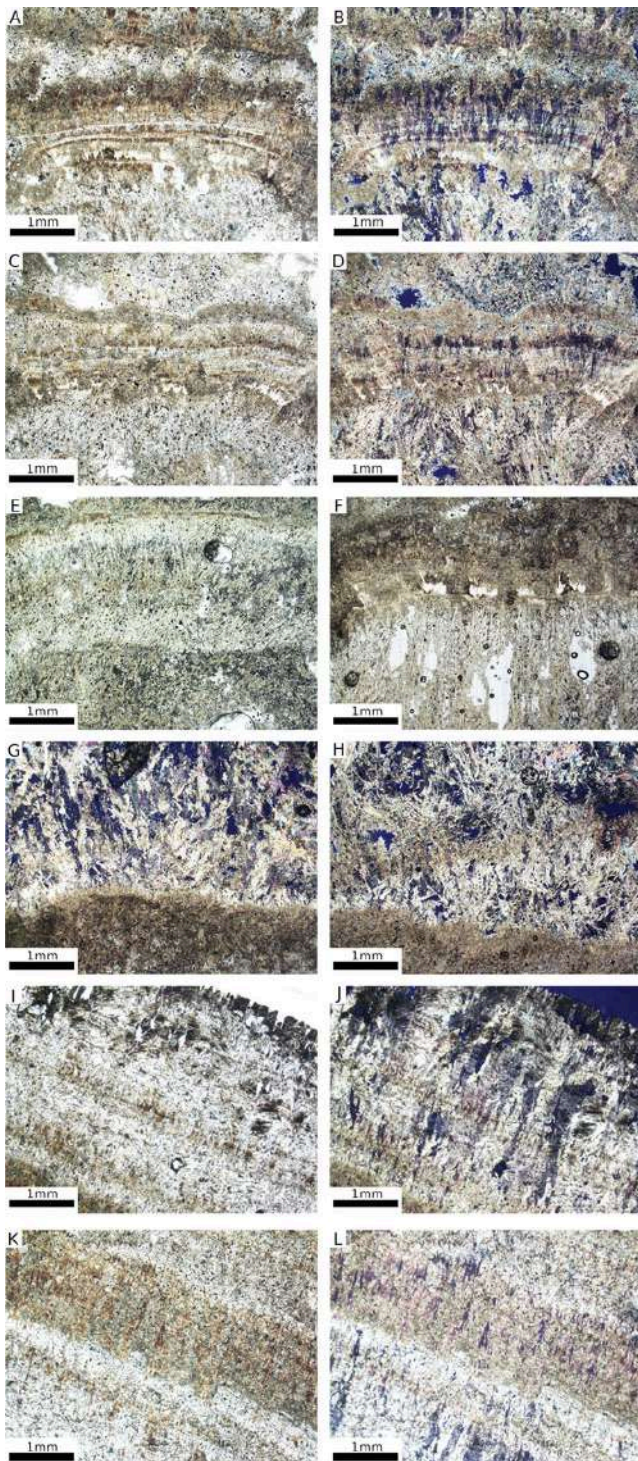


**Fig. 6.** Microfabrics of the studied flowstone. A, B, C, D: alternation of dendritic and compact columnar calcite in the sub-vertical segments of the flowstone (A, C = parallel nicols, B, D = crossed nicols); E, F, G, H: dendritic calcite, micrite and detritus in sub-vertical segments of the flowstone (E, F = parallel nicols, G, H = crossed nicols); I, J, K, L: compact columnar calcite in the sloped segments of the flowstone (I, K = parallel nicols, J, L = crossed nicols).

and only a couple of samples were in equilibrium respect to calcite, while the other samples were undersaturated (mean  $SI_{\text{calcite}}$  of about  $-0.22$ ). In contrast, during the more stormy events the water had a lower Mg/Ca ratio and was supersaturated with respect to calcite (mean  $SI_{\text{calcite}}$  of about  $0.28$  and  $0.72$  for the first (10th–11th of October) and third (27th October – 4th November) events, respectively). Overall,

the water of the Milano drip site was supersaturated during these storm events, thus favouring calcite precipitation.

The Onda drip site also has a Ca-Mg- $\text{HCO}_3$  composition and shows a decrease in bicarbonate (from  $4.95$  to  $4.81$  meq/l), Ca (from  $3.6$  to  $3.4$  meq/l), and  $SI_{\text{calcite}}$  (from  $1.27$  to  $0.84$ ) downstream along the flowstone, whereas Mg remains rather constant ( $1.55$  to  $1.51$  meq/l).

## 6. Discussion

### 6.1. Hydrodynamic and geochemical environment during the deposition of the wavy flowstone

Stair-case like morphologies are common in speleothems formed by a flowing water film. However, if the supersaturation with respect to calcite is lower than  $\sim 0.25$ , gours are formed (i.e. dammed flowstones

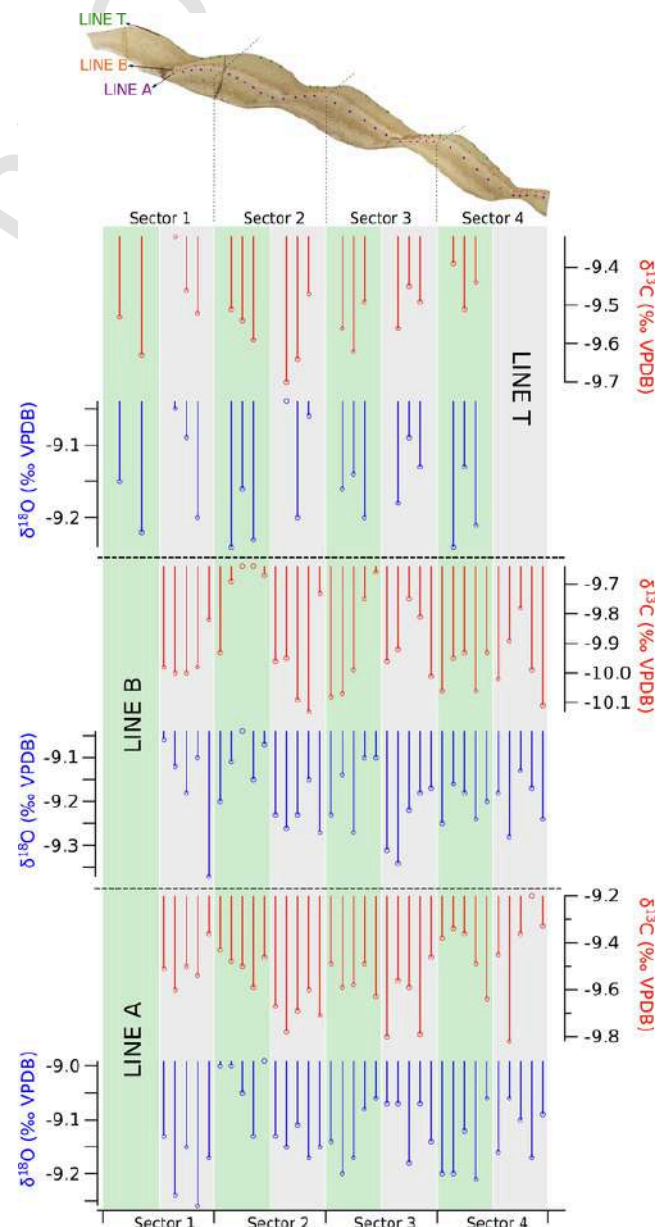


**Fig. 7.** Stable isotope composition along growth layers A, B, and T, from upstream (left) to downstream (right). Green and grey shadings refer to sub-vertical and sloped segments of the flowstone, respectively (see Fig. 3 for the correct orientation of the flowstone). Note the limited variability of  $\delta^{13}\text{C}$  and  $\delta^{18}\text{O}$  along these growth layers. (For interpretation of the references to colour in this figure legend, the reader is referred to the web version of this article.)



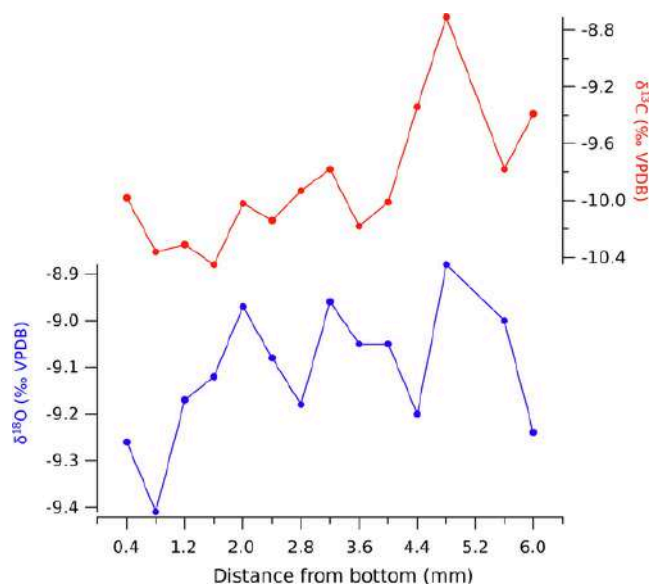


Fig. 8. Stable isotope composition along the transect of line V, that cuts perpendicularly across speleothem growth layers (see Fig. 3 for details of the location of this profile).

or rimstone dams) (Hill and Forti, 1997; Forti and Hill, 2004). Indeed, in this case, the deposition of carbonate is associated with slope irregularities, related to surface roughness. For example, the water film is thinnest and the flow velocity is highest at the edges of surface irregularities, causing the flow transition from laminar to turbulent, which favours carbon dioxide degassing and evaporation, and consequent supersaturation with respect to  $\text{CaCO}_3$  (Buhmann and Dreybrodt, 1985; Meakin and Jamtveit, 2009). With time, a barrier is formed above the inception surface irregularity (Fig. 10). The barriers create a series of pools in which carbonate deposition can also occur. The gourd morphology of flowstones appears genetically similar to surface travertine and calcareous tufa deposits, related to karst springs/streams in both hydrothermal and non-hydrothermal settings (Hammer et al., 2007).

We suggest that the wavy morphology of the studied flowstone has a different origin. In Bossea, there is no formation of a proper “dam”, but calcite covers more or less uniformly the pre-existing relief (Fig. 10). This is possibly due to the supersaturation (SI 0.3 or higher) with respect to calcite (Fig. 9), allowing carbonate deposition to occur uniformly rather than localised, as happens on rimstone dams. As a consequence of the decreasing  $\text{SI}_{\text{calcite}}$ , rimstone pools occur in the distal part of some flowstones.

Wavy flowstones in Bossea cave show that thinner calcite layers are deposited on gently sloped sectors with respect to steep or sub-vertical portions (~1:2 ratio); knickpoints migrate downstream (Fig. 10) and bedrock irregularities, although influencing the early deposition of the basal layers of the flowstones, seem not to interfere with the resulting final regular wavy morphology of the calcite layers. Indeed, the relation between wave slope, length and amplitude of the 16 analysed flowstones (Fig. 5) suggests that the final flowstone architecture is not influenced by random irregularities of the underlying bedrock. In turn, this gives important indications about the flow regime during speleothem formation, i.e. flow was always laminar. A turbulent flow regime would have caused carbonate deposition related to bedrock steps/irregularities, resulting in morphologies characterised by dams or by flowstone balconies (bell canopies). Recent observations suggest that the change from the laminar to turbulent flow regime appears to cause carbonate deposition and “ribbed” morphologies in speleothems (Badino et al., 2017; Forti et al., 2017).

Vesipa et al. (2015) modelled the formation of crenulations on stalagmites, recognising that these morphologies depend on ripple-like in-

stabilities of the calcite–water interface that develop perpendicular to the water film. Their model results in wavelengths (distance between two consecutive ripple crests) of a few centimetres, much shorter than those observed in our wavy flowstones. Another difference is that the flow considered for crenulation formation is much slower than water flowing on actively forming flowstones.

If the water flow never became turbulent, as occurring on some speleothems (Forti et al., 2017), we can envision a homogeneous carbonate-rich water film flowing on the flowstone surface for a certain period of time. According to our field observations in Bossea Cave, water covers the whole flowstone surface as a consequence of heavy, short-lived storms, as those registered the 10th–11th October 2018 and from the 28th October to the 4th November of the same year (Fig. 9). At the Milano (and Onda) station, the  $\text{SI}_{\text{calcite}}$  was well above 0 during these events, which were characterised by rainfall intensities between 10 and 20 mm per hour during rainfall peaks, and average rainfall rates of 7 (10th–11th October) and 3.5 (28th October–4th November) mm/hour. In contrast, during the weaker rainfall on 18th–19th October (< 5 mm/hour during peaks and average rates around 0.8 mm/hour) (Fig. 9), the  $\text{SI}_{\text{calcite}}$  was around or below 0. The Mg/Ca ratio was higher during this last weak rain event, suggesting a different infiltration pattern (Nannoni et al., 2020). During such a low-intensity flow, the water does not form a continuous film, but is rather concentrated in rivulet-like streams draining water on the flowstone surface (Fig. 3) and having possibly an erosive effect on these “channels”. This is the reason why the flowstone is not uniformly convex but interrupted by close-to-vertical, shallow, channel-like features (Fig. 3b). In contrast, during major rainfall events an extensive water film covers the flowstone and calcite deposition occurs across the entire flowstone surface (Fig. 9). The physico-chemical conditions controlling the degree of supersaturation with respect to  $\text{CaCO}_3$ , i.e. the rate of  $\text{CO}_2$  degassing and local evaporation, should be more or less the same across the flowstone. Stable isotope data obtained along individual layers (lines A, B and T) point to such a regime, as shown by the very small range of variation of both  $\delta^{18}\text{O}$  and  $\delta^{13}\text{C}$  (Figs. 7 and 11) and the lack of significant trends (Fig. 11). In fact, there is only a 0.62‰ difference between maximum and minimum  $\delta^{13}\text{C}$  values in line A and less so in the other lines, while maximum and minimum  $\delta^{18}\text{O}$  values in line B differ by 0.33‰ (less so in the other lines). Furthermore,  $\delta^{18}\text{O}$  and  $\delta^{13}\text{C}$  are never correlated along A, B and T lines (Fig. 11). This is also true for the single sub-vertical vs. sloped sectors (Fig. 12).

In caves, calcite deposition can occur under isotopic equilibrium or kinetic fractionation conditions (Hendy, 1971; Kim and O’Neil, 1997). The former is promoted by the availability of the time necessary for a complete isotopic balancing between the water and the solid phase to be achieved. Conversely, kinetic fractionation prevails during the fast nucleation of calcite crystals, which compromises the total equilibration of the solid carbonate phase with respect to the water. Conditions favouring rapid degassing of  $\text{CO}_2$  (and/or rapid evaporation) may provoke non-equilibrium/kinetic fractionation during  $\text{CaCO}_3$  deposition. This is well known in palaeoclimate science, because only speleothems deposited under equilibrium conditions faithfully preserve the isotopic signature of seepage water and hence of meteoric precipitation (Fairchild and Baker, 2012). For example, stalagmites are regarded as formed at isotopic equilibrium if  $\delta^{18}\text{O}$  and  $\delta^{13}\text{C}$  are not positively correlated and do not increase from the centre to the side along individual lamina (Hendy, 1971). Regarding the last point, a maximum enrichment threshold of 0.8‰ is usually taken as reference (Gascogne, 1992). Thus, the so-called Hendy test (Hendy, 1971) is used to assess the isotopic conditions at the time of speleothem formation at the scale of a single growth layer, which is what we did for lines A, B and T. This test can also be applied to flowstones, by considering  $\delta^{18}\text{O}$  and  $\delta^{13}\text{C}$  values along a single layer. The examined flowstone passes the test. The Hendy test, however, has limitations (Dorale and Liu, 2009; Mühlinghaus et al., 2009; Day and Henderson, 2011), and kinetic controls during car-

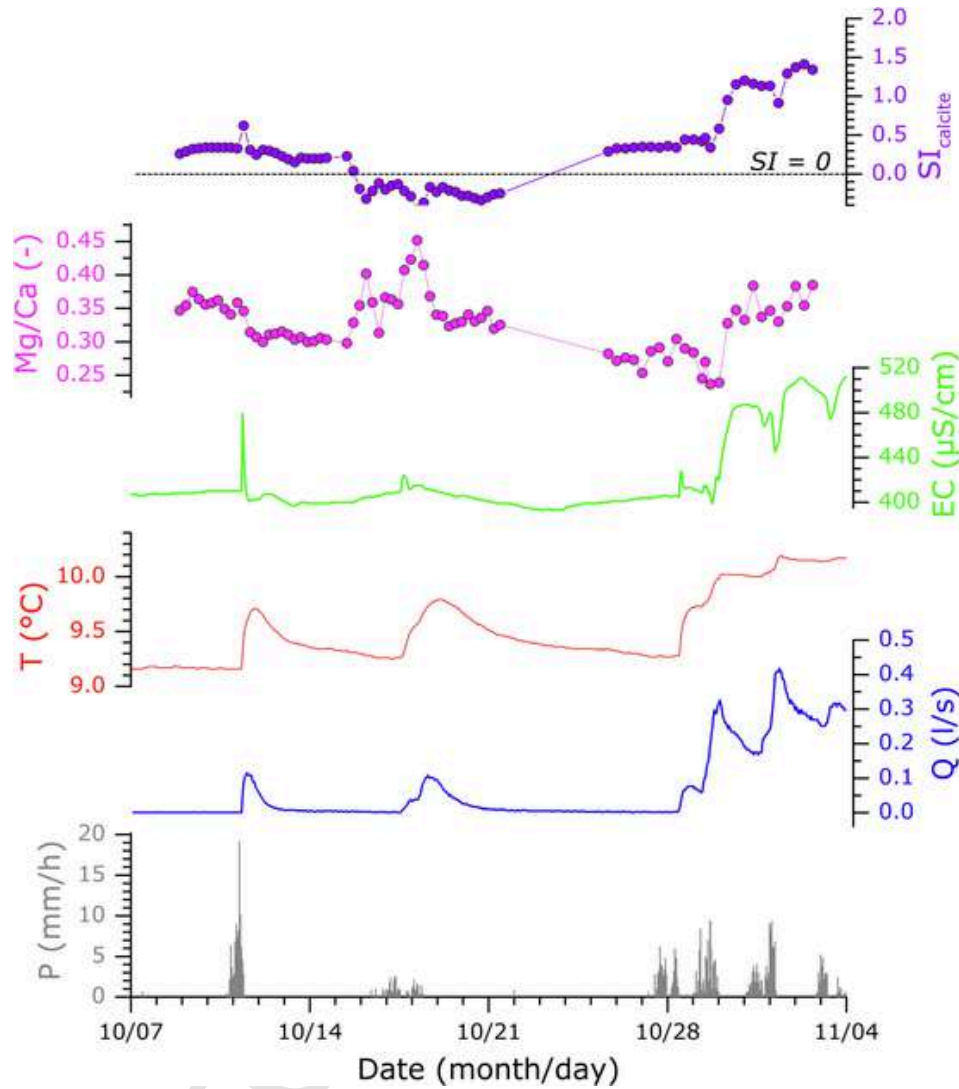


**Fig. 9.** From top to bottom: calcite saturation index ( $SI_{\text{calcite}}$ ), Mg/Ca ratio, electrical conductivity (EC), water temperature (T), discharge (Q), and precipitation (P) of the Milano drip from October 7th to November 4th 2018. Modified after [Nannoni et al. \(2019\)](#).

bonate deposition are more common than previously thought ([Mickler et al., 2006](#); [Wainer et al., 2011](#)). We therefore interpret the flowstone layers sampled in this study as deposited at quasi-equilibrium conditions, as in other studies ([Columbu et al., 2020](#)). This is also in agreement with calcite microfabrics (compact columnar and dendritic calcite), which can be associated to near-equilibrium conditions ([Frisia, 2015](#)). This suggests that laminar flow prevailed during calcite deposition, favouring constant and slow degassing of  $\text{CO}_2$ . The turbulent flow regime was never reached on sub-vertical nor on sloped surfaces.

## 6.2. Modelling the wave morphology

The highly symmetrical pattern of the wavy flowstone ([Fig. 3](#)) suggests that the inception of carbonate deposition was driven by the hydrodynamics along a regular slope, as is the case, for instance, for calcite crenulations ([Vesipa et al., 2015](#); [Camporeale, 2017](#)). As  $\text{CO}_2$  degassing is related to flow velocity, it is likely that surface waves (in flowing water) affect the depositional process and thus the final flowstone architecture.

Here we present a genetic model for the initiation of the wavy geometry, assuming that the free surface hydrodynamics imprint the initial length scale of the pattern. A laminar water film flowing on a flat sloping surface is characterised by water film depth  $\hat{h}_0$  and surface velocity

$\hat{u}_0$  (e.g., [Chang and Demekhin, 2002](#)) given by the following two equations (eq. 1 and 2 respectively):

$$\hat{h}_0 = \left( \frac{3\nu\hat{q}}{g\sin\vartheta} \right)^{1/3}, \quad \hat{u}_0 = \left( \frac{9g\hat{q}^2\sin\vartheta}{8\nu} \right)^{1/3},$$

where the hat refers to dimensional quantities,  $\nu$  is the kinematic viscosity of water,  $g$  is the gravitational acceleration,  $\hat{q}$  is the flow rate per unit span, and  $\vartheta$  is the initially flat bedrock slope ([Fig. 13a](#)). These quantities may be used to scale the full set of hydrodynamic equations (i.e., the Navier-Stokes equations) and eventually obtain a single equation (i.e., the Benney equation, [Benney, 1966](#)) which describes the dynamics of the water-film depth  $h(x, t)$  ([Kalliadasis et al., 2012](#)) (eq. 3):

$$\partial_t h + 2h^2 \partial_x h + \partial_x \left\{ \frac{h^3}{3} \left[ \frac{8}{5} Re h^3 \partial_x h + Re We \partial_{xxx} h - 2 \cot \vartheta \partial_x h \right] \right\} = 0,$$

where  $\partial$  indicates the partial derivative,  $Re = \hat{h}_0 \hat{u}_0 / \nu$  is the Reynolds number, and  $We = \sigma [2 / (g Re^5 \nu^4 \rho \sin \vartheta)]^{1/3}$  is the Weber number being  $\sigma$  and  $\rho$  the surface tension and density of water, respectively. The Benney equation offers the advantage of analytical tractability and it has al-



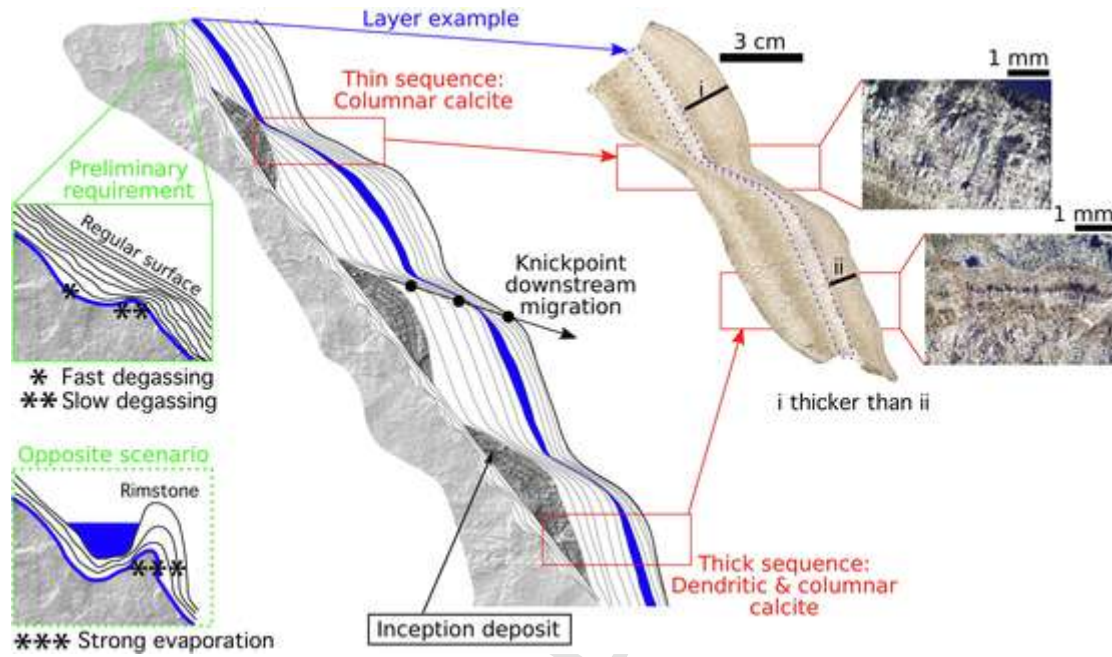


**Fig. 10.** Geometric patterns of wavy flowstones. The preliminary condition leading to a wavy flowstone is a water film flowing on a regular surface. This is due to the smoothing of the initial bedrock slope by carbonate deposition (green box). If the roughness of the bedrock substrate is high a rimstone would form (green dotted box). Inception deposits form across the regular surface (see also Fig. 14 and text for details), leading to the formation of a wavy flowstone. The latter shows a cyclical repetition of thin and thick calcite layers in the downstream direction, composed of columnar only and coupled columnar and dendritic calcite, respectively. (For interpretation of the references to colour in this figure legend, the reader is referred to the web version of this article.)

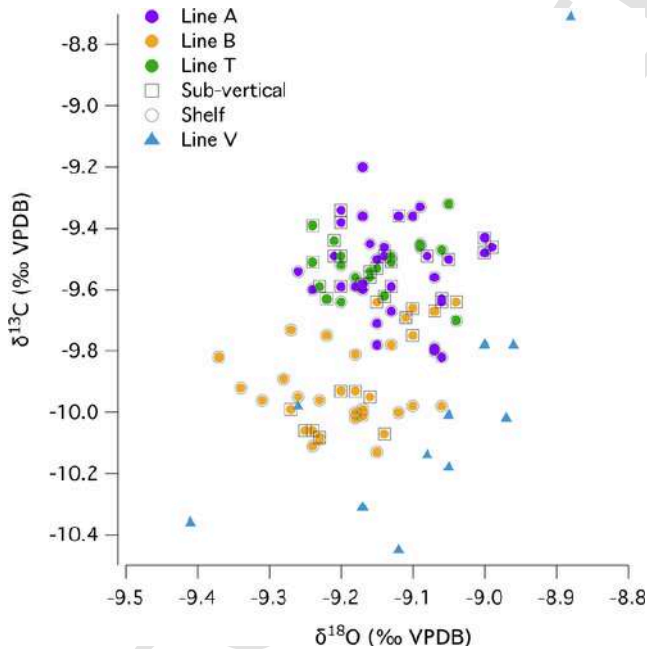


**Fig. 11.** Relationship between  $\delta^{18}\text{O}$  and  $\delta^{13}\text{C}$  values for sub-vertical and sloped surfaces (line A, B and T) and the horizontal transect (line V).

ready been effectively used within the context of speleothem formation (e.g., Bertagni and Camporeale, 2017, Camporeale, 2017).

A standard linear stability analysis of the Benney equation (e.g., Kalliadasis et al., 2012) around the flat base state ( $h = 1$ ) reveals that surface roll waves form for  $Re > Re_c = 5 \cot \theta / 4$  with a dimensional wavelength  $\hat{\lambda}$  given by the equation (eq. 4):

$$\hat{\lambda} = \frac{2\pi\sqrt{ReWe}}{\sqrt{4Re/5 - \cot \theta}} \hat{h}_0 [m]$$

Another key feature of the roll waves is their migration. A single wavelength moves downstream during a time  $\hat{T}_{wave} = \hat{\lambda}/\hat{c}$ , where  $\hat{c} = 2\hat{u}_0$  known as the wave celerity. Our fundamental hypothesis is that the roll waves can affect the water-calcite boundary and the pattern formation if  $\hat{T}_{wave}$  is larger than the typical diffusion timescale of the calcium carbonate system, namely  $\hat{T}_{diff} = (\hat{h}_0/2)^2/D$ , where  $D \approx 10^{-5} \text{ cm}^2/\text{s}$  is the diffusivity of  $\text{Ca}^{2+}$  and  $\text{CO}_2$  in water, and  $\hat{h}_0/2$  is the average diffusive path. If this condition is not satisfied, then the wave dynamics is too fast to affect the depositional process.

Fig. 13b shows that the condition  $\hat{T}_{wave} \geq \hat{T}_{diff}$  is satisfied for a small range of  $Re$ , from the lower limit  $Re = Re_c$ , which defines the incipient formation of surface waves, to  $Re = Re_T$ , corresponding to the condition  $\hat{T}_{wave} = \hat{T}_{diff}$ . Therefore, only a very narrow range of Reynolds numbers guarantees a successful feedback between free-surface dynamics and the calcite depositional process. Fig. 13c shows  $Re_T - Re_c$  versus the sloping of the wall  $\theta$ . This range is basically zero for  $\theta$  less than  $30^\circ$ , i.e., there are no possible flows producing ripples in the water surface at those angles, a result that might explain why wavy flowstone patterns have been observed mainly on steep (greater than  $30^\circ$ ) bedrock slopes. Since for  $Re > Re_T$ , the surface waves are too fast to feed the solid-water interface via diffusion, at higher flow rates  $Re_T$  can be considered the highest formative flow rate for the incipient formation of the pattern. The corresponding wavelength  $\hat{\lambda}$  is reported as a function of the angle  $\theta$  in panel d of Fig. 13d, along with observed averaged data for the 16 flowstones profiles analysed. There is some overlap despite the simplicity of the approach. Although the present framework is heuristic, it is remarkable in reproducing some observations, i.e., it possibly explains why no patterns arise on gentle slopes and it adequately reproduces the regular wavelength of the patterns. A more complete theory, which properly accounts for the hydrodynamics and biogeochemistry

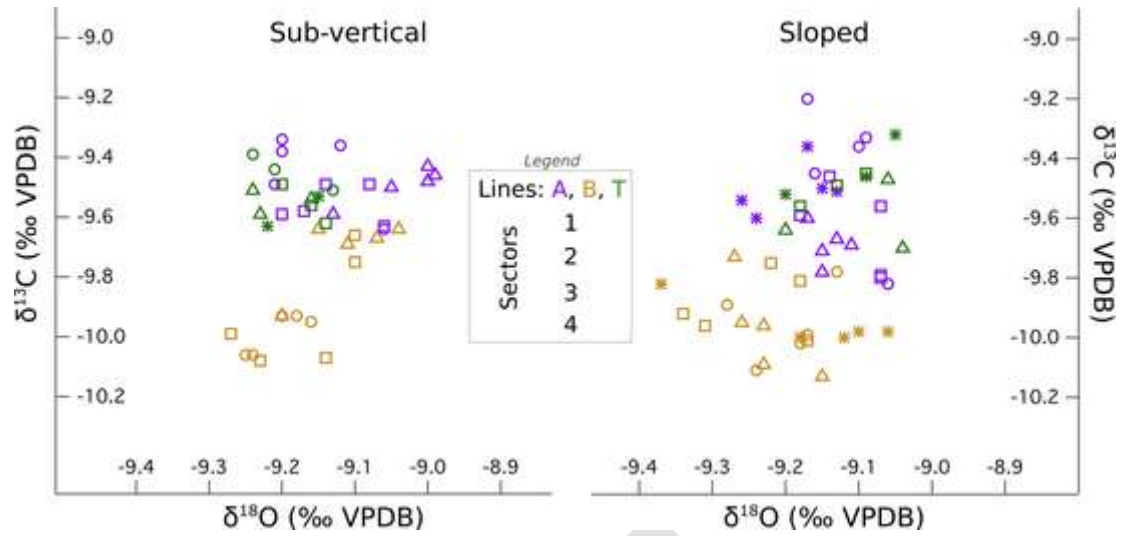


Fig. 12. Relationship between  $\delta^{18}\text{O}$  and  $\delta^{13}\text{C}$  values for sub-vertical and sloped surfaces in different sectors (for sector locations refer to Fig. 3).

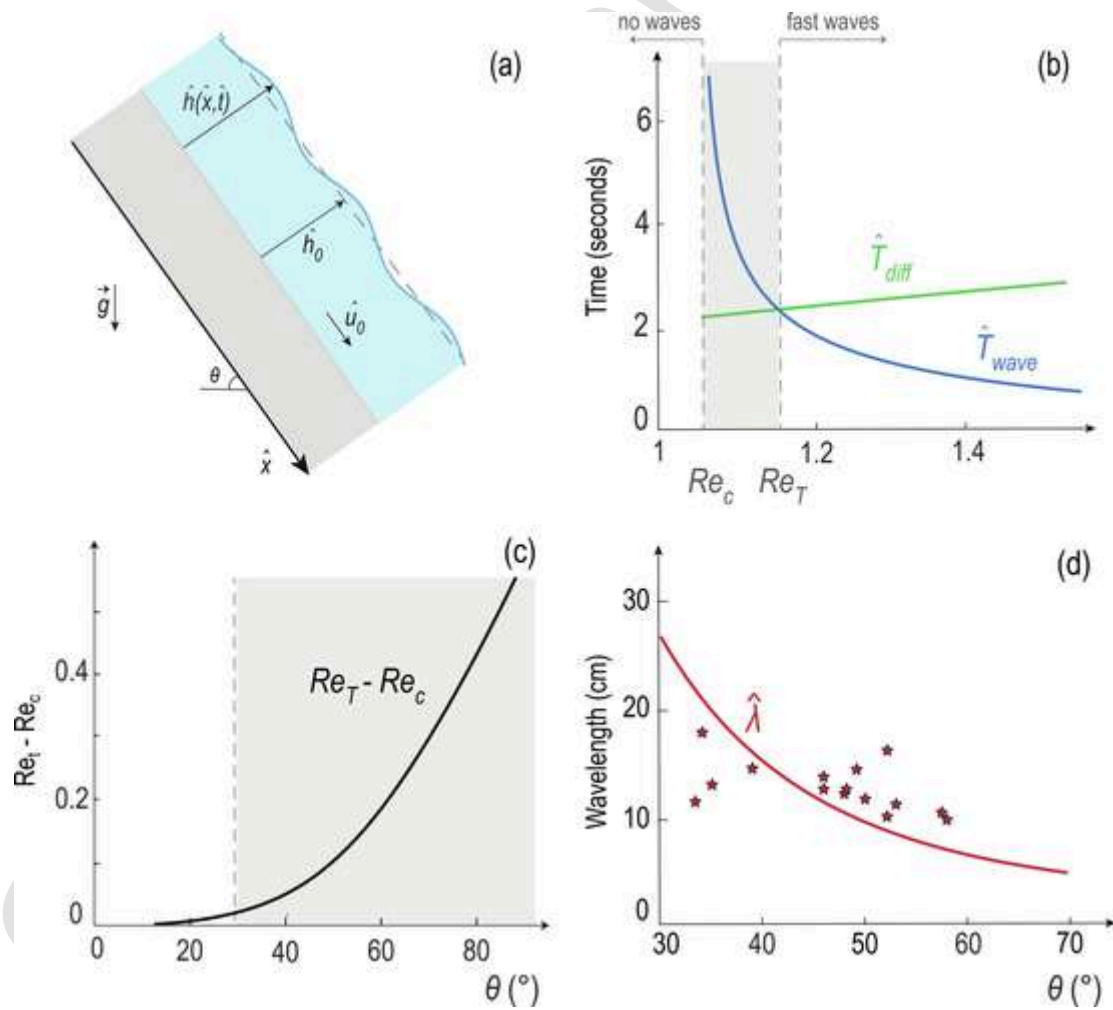


Fig. 13. Model. (a) Sketch of the model and its variables. (b) Timescale of the moving roll waves ( $\hat{T}_{\text{wave}}$ ) and the diffusive vertical process ( $\hat{T}_{\text{diff}}$ ). Formative conditions (grey area) are for Reynolds numbers  $Re_T < Re < Re_c$ , i.e. when  $\hat{T}_{\text{wave}} > \hat{T}_{\text{diff}}$ . (c)  $Re_T - Re_c$  versus the slope  $\theta$ . Formative conditions (grey area) start to occur for slope angles  $\theta \gtrsim 30^\circ$ . (d) Wavelength of the free-surface roll waves — solid line from eq. 3 — compared to field observation of the cave patterns (parameters from Fig. 5c).

of the oversaturated water, may provide further insights into the physical processes that govern these regular patterns.

### 6.3. Hydroclimate-driven formation of wavy flowstones

The model presented above explains the deposition of calcite on a regularly sloping surface, resulting in a symmetrical pattern (Fig. 3). The original slope on which deposition started was irregular, and its morphology was strongly influenced by the erosion of the metavolcanic rocks by the Mora Creek and consecutive slope movements. In Bossea Cave, the geomechanical properties of the metavolcanics naturally lead to rather smooth, slightly irregular and steep slopes, as observed where these rocks outcrop within the cave. The initial calcite deposition on such unevenly steep slopes is mainly influenced by the rate of  $\text{CO}_2$  diffusion, which largely depends on the thickness of the water film. Evaporation of the flowing water films is excluded here, since the relative humidity of the cave air is always very close to 100%. On a slope with small irregularities (Fig. 10) the film thickness mainly depends on the

combination of slope angle and flow velocity (as also shown in eq. 1 and 2). Steeper parts will thus be characterised by more enhanced  $\text{CO}_2$  degassing (and thus calcite deposition), more gentle portions will witness lower calcium deposition rates. If no turbulence and no evaporation occur, these irregular parts will be gradually smoothed leading to a regular sloping surface. If bedrock roughness is preponderant, however, turbulence may occur favouring calcite deposition in these protruding parts, giving rise to the formation of rimstone dams (Fig. 10).

Once water flows on a semi-regular surface (Fig. 14), defined as  $t = 0$ , carbonate deposition is then mainly driven by the interference between the surface of the water and the cave atmosphere (i.e. forming water surface ripples) (Fig. 13a and Fig. 14a) leading to  $\text{CO}_2$  degassing, as known from calcite crenulations (Vesipa et al., 2015; Camporeale and Ridolfi, 2012). At  $t = 0$ , a water film saturated with respect to  $\text{CaCO}_3$  reaches supersaturation because of the instability of these waves, depositing a higher amount of carbonate in specific areas with a symmetrical spacing (Fig. 14b). Deposition of the inception layers (Fig. 10, called “inception deposit”) occurs across the whole surface, because

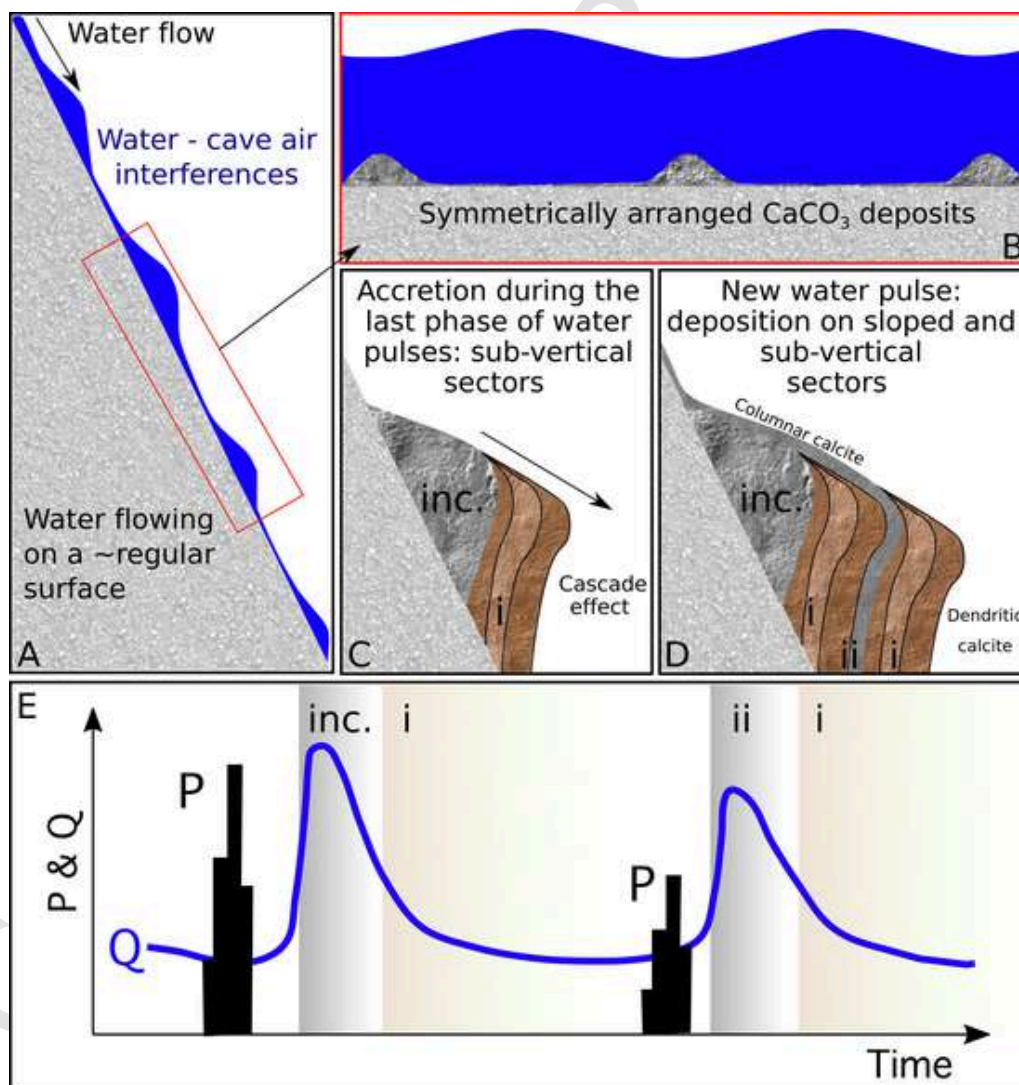


**Fig. 14.** Model of the wavy flowstone formation. A) Laminar flow of  $\text{CaCO}_3$ -rich water along a regular surface (see Fig. 10) at  $t = 0$ ; B) deposition of  $\text{CaCO}_3$  results in symmetrical features (inception deposits “inc.”, see also Fig. 10) because it is driven by water-cave atmosphere interferences, as reported for calcite crenulations (Vesipa et al., 2015); C) During later phases, deposition is limited to the edge of the sloped portions, because of the cascade effect. Prolonged  $\text{CO}_2$  degassing causes the deposition of dendritic calcite on sub-vertical sectors (scenario “i”); D) A subsequent pulse of laminar flow results in the deposition of columnar calcite on both sloped and sub-vertical surfaces (scenario “ii”). The late phase of this pulse is represented by dendritic calcite on sub-vertical sectors (scenario “i”). Subsequent water pulses would result in bundles of columnar calcite overlain by dendritic calcite. E) Variations of idealised parameters ( $P$  = rainfall precipitation;  $Q$  = discharge) through time, leading to the different scenarios (inc. = inception deposits; i = cascade effect and deposition of dendritic calcite; ii = laminar flow and deposition of columnar calcite).



the latter is totally covered by the water film during storm-related infiltration events (high rainfall, Fig. 9). During these events the  $\text{CaCO}_3$  concentration reaches 302 mg/l on the highest part of the flowstone and 294 mg/l at its lowest. These initial deposits of calcite on the bedrock slopes influence the deposition of the subsequent layers (Fig. 14c, d), acting as symmetrical-spaced irregularities where supersaturation with respect to calcite is selectively favoured. The final flowstone morphology inherits the pattern originated by the water surface-air interference (i.e. water ripples).

During a subsequent major infiltration event, the laminar water film covers the entire flowstone surface again, and compact columnar calcite is deposited (Fig. 14d) on both sub-vertical (Fig. 6a–d and Fig. 10) and sloped (Fig. 6i–l and Fig. 10) surfaces, because of the supersaturation with respect to  $\text{CaCO}_3$  given by the slow  $\text{CO}_2$  degassing. After this first layer of columnar calcite, the carbonate content of the water is reduced because  $\text{CaCO}_3$  and  $\text{P}_{\text{CO}_2}$  are reduced, and water velocity slows down because the recharge is decreasing. The latter is testified by the presence of fine-grained detrital particles trapped on the columnar calcite layer (Fig. 6e–h). At this stage, water can still reach supersaturation with respect to calcite, but deposition is now limited to the edge of the pre-formed sloped layers (Fig. 14c), because of the cascade effect. The latter forces  $\text{CO}_2$  degassing, triggering supersaturation with respect to  $\text{CaCO}_3$ . This is demonstrated by i) the thickness of sub-vertical compared to sloped portions, ii) the downstream migration of knickpoints, and iii) the downlap-like terminations of sub-vertical sectors onto sloped ones. Because of these small cascades, prolonged  $\text{CO}_2$  degassing occurs in sub-vertical sectors (the latter is supported by the co-variance between  $\delta^{18}\text{O}$  and  $\delta^{13}\text{C}$  in line V, Fig. 8), and dendritic fabrics prevail. These fabrics are commonly associated with prolonged degassing and growth inhibition by impurities (Frisia and Borsato, 2010; Frisia 2015). Samples of the porous dendritic layers (line V) show a weak increase in  $\delta^{18}\text{O}$  with respect to the other lines (Fig. 11), as previously reported for this fabric (Frisia, 2015; Chiarini et al., 2017).

With respect to the conditions leading to more compact fabrics, dendritic layers are usually associated with a drier climate, when enhanced degassing and evaporation prevail and result in higher  $\delta^{18}\text{O}$  and  $\delta^{13}\text{C}$  values (McDermott et al., 1999). However, line  $\delta^{13}\text{C}$  values of V are not affected by such enrichment, but generally appear more negative than the average values of the other lines (Fig. 11). If  $\delta^{13}\text{C}$  values of dendritic calcite are more negative than those of compact calcite, kinetic processes likely did not alter the original isotopic signature of the feeding water and  $\delta^{13}\text{C}$  values are recording rainfall and/or soil-related signals (Frisia, 2015). It has also been reported that microorganisms could be responsible of dendritic calcite formation (Jones and Kahle, 1993; Banks et al., 2010), because they trigger degassing and evaporation. We do not have evidence of microbial presence in our sample, although the humid environment and the slow flow during dendritic calcite deposition could be a suitable habitat. However, biotic or abiotic-driven degassing/evaporation would not significantly affect the proposed model of wavy flowstone deposition.

At the end of the water pulse, the flowstone consists of layers of compact calcite on sloped surfaces and an alternation of dendritic and columnar calcite on sub-vertical surfaces (Fig. 14d). A new storm-related infiltration event would possibly produce another  $\text{CaCO}_3$ -rich laminar flow film, in turn depositing a layer of compact calcite covering the whole speleothem, i.e. both sloped and sub-vertical surfaces. In this case, the wavy morphology does not influence the carbonate deposition, because the water is sufficiently supersaturated with respect to  $\text{CaCO}_3$  and deposition is uniform. However, the later stages of this new water pulse would result in dendritic calcite deposition in sub-vertical sectors only. The cyclical repetition of these processes gives rise to the wavy flowstone morphology.

#### 6.4. Palaeoclimate implications

Symmetrically wavy flowstones witness wet seasons characterised by short episodes of high rainfall. In currently (semi)arid areas and/or in regions where extreme precipitation events are rare, these speleothems indicate that the seasonal distribution of rainfall has changed. In accordance, dating these speleothems provides precise chronological constraints on this hydroclimate shift. Concurrently, lack of deposition (i.e. hiatus) along an apparently continuous flowstone sequence or changes in the fabric point to periods when storm events temporarily ceased. In Bossea cave, periods characterised by a lower amount of rainfall during the wet season produced moonmilk, similar to other Italian Alpine caves (Borsato et al., 2000); constraining multiple hiatuses and/or moonmilk layers in a speleothem stratigraphy would allow to identify drier than usual climate periods in the past. This is a powerful approach in areas affected by aridity due to climate change, as it provides a baseline of natural climate variability.

To the best of our knowledge, U-Th dating has not been applied to wavy flowstone formations. We regard the compact calcite layers as the most suitable samples for dating, because: i) they contain less detritus compared to the porous layers; ii) diagenetic processes, which would re-open the U-Th geochemical system and thus compromise the reliability of the analyses (Bajo et al., 2016), are less likely to occur within the compact calcite with respect to the porous one. Dating compact calcite layers should allow to constrain the timing of episodes of abundant rainfall in the past, providing insights into the cyclicity of such precipitation events. This would procure a comparison with the recent instrumental precipitation record that shows an alarming increase of rainfall events and long dry spells (Brunetti et al., 2004). Heavy storms are more often causing flash floods in highly populated Mediterranean areas, where numerous cities especially in Italy had numerous casualties and/or damages. A better understanding of the long-term dynamics of heavy precipitation events will help to improve future climate scenarios involving extreme events. Wavy flowstones could be a useful new tool to achieve this aim.

#### 7. Conclusions

This work presents a multidisciplinary study of wavy flowstones, a peculiar cave carbonate deposit. Morphological, fabric and stable isotope analyses show that its symmetrical architecture is not due to pre-existing bedrock irregularities. The proposed evolutionary model emphasises hydrodynamic processes as key for the distinctive wavy morphology. Calcite deposition occurs when a thin water film supersaturated with respect to  $\text{CaCO}_3$  covers the entire flowstone. In Bossea cave, this only occurs following major rain events (with rates higher than 3.5 mm/h). We propose that flowstones showing a regular wavy morphology are promising hydroclimate archives in order to gain insights into the temporal distribution of extreme precipitation events.

#### Uncited references

Columbu et al., 2019; Kalnauasis et al., 2012.



#### Declaration of Competing Interest

The authors declare that they have no known competing financial interests or personal relationships that could have appeared to influence the work reported in this paper: [Andrea Columbu reports equipment, drugs, or supplies was provided by University of Innsbruck. Andrea Columbu reports equipment, drugs, or supplies was provided by Polytechnic of Turin.].



## Acknowledgments

We would like to thank Dr. Fabio Gamberini for the preparation of thin sections and Professors Giulio Viola and Paolo Garofalo for the access to the Deformation, Fluids and Tectonics Laboratory (BiGeA Department, Bologna University), as well as Fabrizio Bianco (Water chemistry laboratory, DIATI department, Polytechnic of Turin) for water analyses. Finally, we are grateful to Andrea Martín Pérez and two anonymous reviewers for their insightful comments.

## Appendix A. Supplementary material

Supplementary data to this article can be found online at <https://doi.org/10.1016/j.catena.2022.106294>.

## References

- Antonellini, M., Nannoni, A., Vigna, B., De Waele, J., 2019. Structural control on karst water circulation and speleogenesis in a lithological contact zone: The Bossea cave system (Western Alps, Italy). *Geomorphology* 345, 106832. <https://doi.org/10.1016/j.geomorph.2019.07.019>.
- Atsawawaranunt, K., Comas-Bru, L., Amirnezhad Mozhdehi, S., Deininger, M., Harrison, S.P., Baker, A., Boyd, M., Kaushal, N., Ahmad, S.M., Ait Brahim, Y., Arienzo, M., Bajo, P., Braun, K., Burstyn, Y., Chawchai, S., Duan, W., Hatvani, I.G., Hu, J., Kern, Z., Labuhn, I., Lachniet, M.S., Lechleitner, F.A., Lorrey, A., Pérez-Mejías, C., Pickering, R., Scroton, N., 2018. The SISAL database: a global resource to document oxygen and carbon isotope records from speleothems. *Earth Syst. Sci. Data* 10 (3), 1687–1713.
- Badino, G., Calaforra, J.M., De Waele, J., Forti, P., 2017. A hypothesis on the evolution of complex flowstones. In: *Proceedings 17th International Speleological Congress*. pp. 320–324.
- Bajo, P., Hellstrom, J., Frisia, S., Drysdale, R., Black, J., Woodhead, J., Borsato, A., Zanchetta, G., Wallace, M.W., Regattieri, E., 2016. “Cryptic” diagenesis and its implications for speleothem geochronologies. *Quat. Sci. Rev.* 148, 17–28.
- Banks, E.D., Taylor, N.M., Gulley, J., Lubbers, B.R., Giarrizzo, J.G., Bullen, H.A., Hoehler, T.M., Barton, H.A., 2010. Bacterial calcium carbonate precipitation in cave environments: a function of calcium homeostasis. *Geomicrobiol. J.* 27 (5), 444–454.
- Banzato, C., Marchionatti, F., Vigna, B., 2013. Drainage index calculated with artificial tracers. *AQUA Mundi* 67–75. <https://doi.org/10.4409/Am-059-13-0053>.
- Benney, D.J., 1966. Long waves on liquid films. *J. Math. Phys.* 45 (1–4), 150–155.
- Bertagni, M.B., Camporeale, C., 2017. Nonlinear and subharmonic stability analysis in film-driven morphological patterns. *Phys. Rev. E* 96 (5), 053115.
- Borsato, A., Frisia, S., Jones, B., Van Der Borg, K., 2000. Calcite moonmilk: crystal morphology and environment of formation in caves in the Italian Alps. *J. Sediment. Res.* 70 (5), 1171–1182.
- Brunetti, M., Buffoni, L., Mangianti, F., Maugeri, M., Nanni, T., 2004. Temperature, precipitation and extreme events during the last century in Italy. *Global Planet. Change* 40, 141–149.
- Buhmann, D., Dreybrodt, W., 1985. The kinetics of calcite dissolution and precipitation in geologically relevant situations of karst areas: 1. Open system. *Chem. Geol.* 48 (1–4), 189–211.
- Camporeale, C., 2017. An asymptotic approach to the crenulation instability. *J. Fluid Mech.* 826, 636.
- Camporeale, C., Ridolfi, L., 2012. Hydrodynamic-driven stability analysis of morphological patterns on stalactites and implications for cave paleoflow reconstructions. *Phys. Rev. Lett.* 108 (23), 238501.
- Chang, H.H., Demekhin, E.A., 2002. Complex wave dynamics on thin films. Elsevier.
- Cheng, H., Edwards, R.L., Sinha, A., Spötl, C., Yi, L., Chen, S., Kelly, M., Kathayat, G., Wang, X., Li, X., Kong, X., 2016. The Asian monsoon over the past 640,000 years and ice age terminations. *Nature* 534, 640–646.
- Chiarini, V., Couchoud, I., Drysdale, R., Bajo, P., Milanolo, S., Frisia, S., Greig, A., Hellstrom, J., De Waele, J., 2017. Petrographical and geochemical changes in Bosnian stalagmites and their palaeo-environmental significance. *Int. J. Speleol.* 46 (1), 33–49.
- Columbu, A., Spötl, C., De Waele, J., Yu, T.L., Shen, C.C., Gázquez, F., 2019. A long record of MIS 7 and MIS 5 climate and environment from a western Mediterranean speleothem (SW Sardinia, Italy). *Quat. Sci. Rev.* 220, 230–243.
- Columbu, A., Chiarini, V., Spötl, C., Benazzi, S., Hellstrom, J., Cheng, H., De Waele, J., 2020. Speleothem record attests to stable environmental conditions during Neanderthal-Modern Human turnover in Southern Italy. *Nat. Ecol. Evol.* 4 (9), 1188–1195.
- Columbu, A., Calabrò, L., Chiarini, V., De Waele, J., 2021. Stalagmites: from Science Application to Museumization. *Geohistory* 13, 47.
- Curl, R.L., 1973. Minimum diameter stalagmites. *Bull. Natl. Speleol. Soc.* 35, 1–9.
- Day, C.C., Henderson, G.M., 2011. Oxygen isotopes in calcite grown under cave-analogue conditions. *Geochim. Cosmochim. Acta* 75 (14), 3956–3972.
- Dorale, J.A., Liu, Z., 2009. Limitations of Hendy test criteria in judging the paleoclimatic suitability of speleothems and the need for replication. *J. Cave Karst Stud.* 71 (1), 73–80.
- Dreybrodt, W., Romanov, D., 2008. Regular stalagmites: the theory behind their shape. *Acta Carsologica* 37 (2–3), 175–184.
- Drysdale, R.N., Couchoud, I., Zanchetta, G., Isola, I., Regattieri, E., Hellstrom, J., Govin, A., Tzedakis, P.C., Ireland, T., Corrick, E., Greig, A., Wong, H., Piccini, L., Holden, P., Woodhead, J., 2020. Magnesium in subaqueous speleothems as a potential palaeotemperature proxy. *Nat. Commun.* 11 (1), 1–11. <https://doi.org/10.1038/s41467-020-18083-7>.
- Fairchild, I.J., Baker, A., 2012. *Speleothem science: from process to past environments*. John Wiley and Sons.
- Fairchild, I.J., Smith, C.L., Baker, A., Fuller, L., Spötl, C., Matthey, D., McDermott, F., 2006. Modification and preservation of environmental signals in speleothems E.I.M.F. *Earth-Sci. Rev.* 75 (1–4), 105–153.
- Forti, P., Hill, C., 2004. *Speleothems*. In: Gunn, J. (Ed.), *Encyclopedia of Caves and Karst Sciences*. Fitzroy Dearborn, London, pp. 1476–1486.
- Forti, P., Badino, G., Calaforra, J.M., De Waele, J., 2017. The ribbed drapery of the Puerto Princesa Underground River (Palawan, Philippines): morphology and genesis. *Int. J. Speleol.* 46 (1), 93–97.
- Frisia, S., 2015. Microstratigraphic logging of calcite fabrics in speleothems as tool for palaeoclimate studies. *Int. J. Speleol.* 44 (1), 1–16.
- Frisia, S., Borsato, A., 2010. Karst. In: Alonso-Zarza A.M., Tanner L.H. (Eds.), *Carbonates in continental settings. Developments in Sedimentology*, Vol. 61, pp. 269–318.
- Gascoyne, M., 1992. Palaeoclimate determination from cave calcite deposits. *Quat. Sci. Rev.* 11 (6), 609–632.
- Gázquez, F., Columbu, A., De Waele, J., Breitenbach, S.F., Huang, C.-R., Shen, C.-C., Lu, Y., Calaforra, J.-M., Vautravers, M.J.M., Hodel, D.A., 2018. Quantification of paleo-aquifer changes using clumped isotopes in subaqueous carbonate speleothems. *Chem. Geol.* 493, 246–257.
- Hammer, Ø., Dysthe, D., Jamtveit, B., 2007. The dynamics of travertine dams. *Earth Planet. Sci. Lett.* 256 (1–2), 258–263.
- Hellstrom, J., 2006. U-Th dating of speleothems with high initial  $^{230}\text{Th}$  using stratigraphical constraint. *Quat. Geochronol.* 1 (4), 289–295.
- Hellstrom, J., McCulloch, M.T., 2000. Multi-proxy constraints on the climatic significance of trace element records from a New Zealand speleothem. *Earth Planet. Sci. Lett.* 179, 287–297.
- Henderson, G.M., 2006. Climate. Caving in to new chronologies. *Science* 313, 620–622.
- Hendy, C.H., 1971. The isotopic geochemistry of speleothems-I. The calculation of the effects of different modes of formation on the isotopic composition of speleothems and their applicability as palaeoclimatic indicators. *Geochim. Cosmochim. Acta* 35 (8), 801–824.
- Hill, C.A., Forti, P., 1997. *Cave Minerals of the World* (2nd ed.). National Speleological Society.
- Jones, B., Kahle, C.F., 1993. Morphology, relationship, and origin of fiber and dendrite calcite crystals. *J. Sediment. Res.* 63 (6), 1018–1031.
- Kalliadasi, S., Ruyter-Quil, C., Scheid, B., Velarde, M.G., 2012. *Falling liquid films*. Applied Mathematical Sciences, Springer Science and Business Media.
- Kim, S.-T., O’Neil, J.R., 1997. Equilibrium and nonequilibrium oxygen isotope effects in synthetic carbonates. *Geochim. Cosmochim. Acta* 61 (16), 3461–3475.
- Koltai, G., Cheng, H., Spötl, C., 2018. Palaeoclimate significance of speleothems in crystalline rocks: a test case from the Late Glacial and early Holocene (Vinschgau, northern Italy). *Clim. Past* 14 (3), 369–381.
- Lachniet, M.S., 2009. Climatic and environmental controls on speleothem oxygen-isotope values. *Quat. Sci. Rev.* 28 (5–6), 412–432.
- Lechleitner, F., Amirnezhad-Mozhdehi, S., Columbu, A., Comas-Bru, L., Labuhn, I., Pérez-Mejías, C., Rehfeld, K., 2018. The potential of speleothems from western Europe as recorders of regional climate: a critical assessment of the SISAL database. *Quaternary* 1 (3), 30.
- Martín-Chivelet, J., Muñoz-García, M.B., Cruz, J.A., Ortega, A.I., Turrero, M.J., 2017. *Speleothem Architectural Analysis: Integrated approach for stalagmite-based palaeoclimate research*. Sed. Geol. 353, 28–45.
- McDermott, F., Frisia, S., Huang, Y., Longinelli, A., Spiro, B., Heaton, T.H.E., Hawkesworth, C., Borsato, A., Keppens, E., Fairchild, I.J., van der Borg, K., Verheyden, S., Selmo, E., 1999. Holocene climate variability in Europe: Evidence from  $\delta^{18}\text{O}$ , textural and extension-rate variations in three speleothems. *Quat. Sci. Rev.* 18, 1021–1038.
- Meakin, P., Jamtveit, B., 2009. Geological pattern formation by growth and dissolution in aqueous systems. *Proc. Roy. Soc. A: Math. Phys. Eng. Sci.* 466, 659–694.
- Mickler, P.J., Stern, L.A., Banner, J.L., 2006. Large kinetic isotope effects in modern speleothems. *GSA Bull.* 118 (1–2), 65–81.
- Moore, G., 1952. Speleothem—a new cave term. *Natl. Speleol. Soc. News* 10 (6), 2.
- Mühlinghaus, C., Scholz, D., Mangini, A., 2009. Modelling fractionation of stable isotopes in stalagmites. *Geochim. Cosmochim. Acta* 73 (24), 7275–7289.
- Muñoz-García, M.B., Cruz, J., Martín-Chivelet, J., Ortega, A.I., Turrero, M.J., López-Elorza, M., 2016. Comparison of speleothem fabrics and microstratigraphic stacking patterns in calcite stalagmites as indicators of palaeoenvironmental change. *Quat. Int.* 407, 74–85.
- Nannoni, A., Vigna, B., Fiorucci, A., Spötl, C., De Waele, J., Antonellini, M., 2019. Vadose zone hydrology of an Alpine karst system inferred from dripwater stable isotopes. *Geophys. Res. Abstracts* 21, EGU2019-10803.
- Nannoni, A., Vigna, B., Fiorucci, A., Antonellini, M., De Waele, J., 2020. Effects of an extreme flood event on an alpine karst system. *J. Hydrol.* 590, 125493. <https://doi.org/10.1016/j.jhydrol.2020.125493>.
- Parkhurst, D.L., Appelo, C.A.J., 2013. Description of input and examples for PHREEQC version 3: a computer program for speciation, batch-reaction, one-dimensional transport, and inverse geochemical calculations (No. 6-A43). US Geological Survey.
- Richards, D.A., Dorale, J.A., 2003. Uranium-series chronology and environmental applications of speleothems. *Rev. Mineral. Geochem.* 52 (1), 407–460.
- Sanjurjo-Sánchez, J., Arce Chamorro, C., Vidal Romaní, J., Vaquero-Rodríguez, M., Barrientos, V., Kall, J., 2021. On the genesis of aluminum-rich speleothems in a granite cave of NW Spain. *Int. J. Speleol.* 50 (1), 25–40.

- Vesipa, R., Camporeale, C., Ridolfi, L., Thin-film-induced morphological instabilities over calcite surfaces. In: Proceedings of the Royal Society A: Mathematical, Physical and Engineering Sciences 471 (2015) 20150031.
- Vigna, B., Peano, G., Villavecchia, E., De Waele, J., 2017. The karstological subterranean laboratory of Bossea Cave (N Italy). In: Proceedings of the 17th International Congress of Speleology. pp. 447–451.
- Wainer, K., Genty, D., Blamart, D., Daëron, M., Bar-Matthews, M., Vonhof, H., Dublyansky, Y., Pons-Branchu, E., Thomas, L., van Calsteren, P., Quinif, Y., Caillon, N., 2011. Speleothem record of the last 180 ka in Villars cave (SW France): Investigation of a large  $\delta^{18}\text{O}$  shift between MIS6 and MIS5. *Quat. Sci. Rev.* 30 (1–2), 130–146.
- White, W., 1976. Cave minerals and speleothems. In: Ford, T.D., Cullingford, C.H. (Eds.), *The Science of Speleology*. Academic Press, London, pp. 267–327.

CORRECTED PROOF